ACCEPTED VERSION (J Petrology (2016) 57 (7): 1389-1408)

Effect of water activity on reaction kinetics and intergranular transport: Insights from the $Ca(OH)_2 + MgCO_3 \rightarrow CaCO_3 + Mg(OH)_2$ reaction at 1.8 GPa

Authors

Julien GASC[1]

Laboratoire de Géologie, École normale supérieure, CNRS-UMR8538, Paris, France

Fabrice BRUNET✉

Université Grenoble Alpes, CNRS, ISTERRE, Grenoble, France

Nicolas BRANTUT

Earth Sciences Department, University College London, UK

Jérôme CORVISIER

Centre de Géosciences, Mines ParisTech, Fontainebleau, France

Nathaniel FINDLING

Université Grenoble Alpes, ISTERRE, Grenoble, France

Anne VERLAGUET

ISTeP, – Université Pierre et Marie Curie, 4 place Jussieu, Paris, France

Christian LATHE

GFZ, Telegraphenberg, D-14473 Potsdam, Germany

[1] Current Address: Géosciences Montpellier, Université de Montpellier-CNRS, Montpellier, France

✉ TEL: +33 476 514 106, Fax: +33 476 635 252 e-mail : fabrice.brunet@univ-grenoble-alpes.fr

ABSTRACT

The kinetics of the irreversible reaction $Ca(OH)_2 + MgCO_3 \rightarrow CaCO_3 + Mg(OH)_2$ were investigated at high pressures and temperatures relevant to metamorphic petrology, using both in-situ synchrotron X-ray diffraction and post-mortem analysis of reaction rims growth on recovered samples. Reaction kinetics are found to strongly depend on water content; comparable bulk-reaction kinetics are obtained under water *saturated* (excess water, ca. 10 wt.%) and under *intermediate* (0.1-1 wt.% water) conditions when temperature is increased by ca. 300 K. Whereas, similar reaction kinetics were observed at ~673 K and 823 K between *intermediate* and *dry* experiments, respectively, where *dry* refers to a set of experiments with water activity below one (no free water), as buffered by the $CaO\text{-}Ca(OH)_2$ assemblage. Given the activation energies at play, this gap –corresponding to the loss of no more than 1 wt.% of water by the assemblage– leads to a difference of several orders of magnitude in reaction kinetics at a given temperature.

Further analysis, at the microscopic scale, of the *intermediate* and *dry* conditions samples, shows that intergranular transport of calcium controls the reaction progress. Grain boundary diffusivities could be retrieved from the classic treatment of reaction rim growth rate. In turn, once modeled, this rate was used to fit the bulk kinetic data derived from XRPD, offering an alternative mean to derive calcium diffusivity data. Based on a comparison with effective grain boundary data for Ca and Mg from the literature, it is inferred that both *dry* and *intermediate* datasets are consistent with a water saturated intergranular medium with different levels of connectivity. The very high diffusivity of Ca in the $CaCO_3 + Mg(OH)_2$ rims, in comparison that of Mg in enstatite rims [Gardés et al., *Contributions to Mineralogy and Petrology* 164; 2012], emphasizes the prominent role of the interactions between diffusing species and mineral surfaces on diffusion kinetics. Furthermore, we show that the addition of water is likely to change the relative diffusivity of Mg and Ca in carbonate aggregates. On a qualitative point of view, we confirm, in a carbonate-bearing system, that small water content variations within the 0 - 1 wt. % range, have tremendous effects on both intergranular transport mechanisms and kinetics. We also propose that the water-content dependent diffusivity of major species (Mg, Ca) in low-porosity metamorphic rocks is strongly dependent of the interaction between diffusing species and mineral surfaces. This parameter which will vary from one rock-type to the other, needs also to considered when extrapolating (P,T,t, xH_2O) laboratory diffusion data to metamorphic processes.

Keywords: metamorphic reaction, kinetics, intergranular transport, water, calcium diffusion

INTRODUCTION

The kinetics of metamorphic reactions is strongly dependent on temperature, grain size and water availability. The latter parameter is probably the most difficult to quantify, especially over the course of a whole metamorphic cycle. The ubiquity of fluid during metamorphism has long been a subject of controversy (Rubie, 1986, Thompson, 1983) and it is widely accepted now that variations of water availability and content, in metamorphic rocks, is likely to account for the discrepancy between natural reaction kinetics and those extrapolated from experimental data (Baxter, 2003). On the field, the prominent role of water availability is supported by occurrences of partially eclogitized high-grade rocks in which eclogitization took place in shear zones, where fluid infiltrated (Austrheim, 1987, John & Schenk, 2003, Molina *et al.*, 2002). At a larger scale, by combining petrological and geophysical constraints, Hetenyi et al. (2007) have suggested that the eclogitization of the Indian lower crust beneath Tibet is delayed due to equilibrium overstepping until it is catalyzed by the release of water from hydrous minerals.

Beyond the notion of water availability, which describes the intermittent presence of water in the course of the metamorphic reaction process, the question of the effect of water content on the reaction kinetics also appears to be relevant. In fact, most of the dataset of mineral reaction kinetics available in the literature (phase relationship, dissolution, etc.) is based on experiments performed under hydrothermal conditions with large water/rock ratios. Consequently, when extrapolated to nature, assuming permanent water availability, this type of experimental data predicts that metamorphic reaction rates are fast and that the preservation of metastable mineral assemblages (reaction equilibrium overstep) is short with respect to metamorphic timescales (Wood & Walther, 1983). Although possibly valid for metapelites transforming along their prograde path, this conclusion does not necessarily hold for high-grade rocks (e.g., upper amphibolite or granulite facies rocks) reacting back with water. Under these latter circumstances, Yardley and Valley (1997) showed, on thermochemical grounds, that excess water conditions (i.e.; water saturation) are not met and that water activity must be below unity (taking as reference state pure water at T and P). In parallel, it has been shown recently that even minute amounts of water can have a drastic effect on the kinetics of mineral reactions through the enhancement of mass transport (Milke *et al.*, 2013; Gardés *et al.*, 2012, Joachim *et al.*, 2012, Carlson, 2010, Milke *et al.*, 2009). In fact, a full range of intergranular diffusion regimes has been identified as a function of water content (Farver & Yund, 1995, Rubie, 1986) between the “dry” and the “water saturated” end member cases. These regimes are characterized by a range of grain boundary diffusivities that can span over seven orders

of magnitude in the case of aluminum (Carlson, 2010). Even though Gardés et al. (2012) proposed a microscopic description for each of these intergranular diffusion regimes, the physical state of water below the 1 wt.% level remains largely unknown under metamorphic pressures and temperatures. Furthermore, studies addressing the effect of low water contents on intergranular transport and its implications for mineral reaction rates are scarce although of high geological relevance. The in-situ characterization at high pressure and temperature (PT) of the physico-chemical properties of intergranular water present in very low concentrations is obviously a difficult task. Gasc et al. (2011), for example, used in-situ impedance spectroscopy at 2 GPa to characterize the electrical properties (diffusivity of electrical charge carriers) of the intergranular region of a brucite polycrystal as a function of temperature for various water contents. Using the $CaO - Ca(OH)_2$ and $MgO - Mg(OH)_2$ equilibria to buffer the water activity in the samples, the authors were able to show that grain-boundary conductivity can vary by seven orders of magnitude upon water content. In the present study, we propose to use a similar water buffering strategy to address the effect of low water content variation on intergranular transport in the course the $Ca(OH)_2 + MgCO_3 \rightarrow CaCO_3 + Mg(OH)_2$ reaction at 1.8 GPa. A special attention will be paid to bridge bulk and microscopic approaches so that reaction kinetics derived from time-resolved x-ray powder diffraction (XRPD) will be compared to growth rate of $CaCO_3 + Mg(OH)_2$ rims around coarse magnetite ($MgCO_3$) grains dispersed in a fine portlandite, $Ca(OH)_2$, matrix. All terms and symbols used throughout the text are defined in Table 1.

EXPERIMENTAL

Experimental strategy

Cubic multi-anvil (DIA) experiments were performed at 1.8 GPa in a range of temperatures (393 – 873 K), run durations and water contents on the non-reversible exchange reaction:

$$Ca(OH)_2 + MgCO_3 \rightarrow Mg(OH)_2 + CaCO_3 \quad (1).$$

This reaction was chosen for its relatively fast kinetics, even under severely dry conditions, in order to allow investigation of its kinetics *in situ* from time-resolved synchrotron diffraction. Additional experiments were also performed in a piston-cylinder (PC) apparatus to investigate the kinetics of reaction (1) under water-saturated conditions at the same pressure, in sealed gold containers.

The recovered MA samples (i.e., *dry* and *intermediate*) were characterized using Scanning Electron Microscopy (SEM) with a Zeiss® Field-effect SEM (FE-SEM), which showed the presence of reaction rims around coarse residual magnesite grains. The kinetics of chemical transport across the rim-forming polycrystalline material, composed of brucite, $Mg(OH)_2$, and aragonite, $CaCO_3$, was characterized from the determination of rim growth rates as well as from one-dimension diffusion experiments performed with the same starting material in the PC apparatus. Grain boundary diffusion coefficients, $\overline{D}^{GB}\delta$, were retrieved from both datasets using a segregation factor set to one, since major element diffusion is involved.

Finally, the two approaches (i.e., bulk reaction kinetics and chemical transport at the reaction rim scale) were bridged. Grain boundary diffusion coefficients were refined to fit the time-resolved synchrotron diffraction data; the diffusion coefficients obtained in this fashion were then compared to those retrieved from the growth rate of reaction rims and reaction fronts (FE-SEM data), in order to test the consistency between microscopic and bulk datasets.

Starting materials

The starting material was a mixture of natural magnesite, $MgCO_3$, and synthetic portlandite, $Ca(OH)_2$. Portlandite was synthesized hydrothermally (623 K, 150 MPa, 45 h) in a cold-seal vessel from CaO, which was obtained by decarbonation of reagent grade calcite (Merck 2066 with <1% impurities) at

1273 K. Magnesite was extracted from a natural single crystal containing less than 1 wt.% CaO and FeO; the absence of mineral impurity was checked by XRPD. Portlandite and magnesite were grinded together in an agate mortar in equimolar proportions. SEM showed that the starting material was composed of a fine-grained matrix (grain diameter less than 1 µm) with, sporadically, coarser magnesite grains (~10 µm). These larger grains are less reactive but, as described hereafter, are suitable for the measurement of reaction rim growth rates.

Reaction kinetics from in-situ synchrotron x-ray diffraction

High PT experiments with in-situ energy dispersive XRPD were carried out using the MAX80 DIA press (6 anvils cubic type multi-anvil) installed on beamline F2.1 at Hasylab. The starting powder was pressed to a pellet (2 mm in diameter) and fitted into a boron nitride (BN) sleeve, which purpose was to insulate chemically the sample from the graphite furnace but was not designed to retain water. The BN sleeve was then fitted into a cylindrical graphite furnace and sandwiched between two dried NaCl pellets used as pressure marker (Decker, 1971). Temperature was measured with a Type-N thermocouple, the junction of which was located at a NaCl / sample interface. Boron-epoxy cubes with 8 mm edges were used as pressure medium in conjunction with 6 mm truncation WC anvils. Details of the cell assembly and the MAX80 press can be found in Mueller (2003). Note that in order to minimize x-ray absorption no sealed noble-metal container was used. Therefore, as described hereafter, water saturated experiments were achieved separately in the PC using sealed gold container.

Two types of hydration levels were tested in the DIA experiments. The starting material was either equilibrated with the air moisture before being loaded into the BN sleeve, or was dried at 383 K and mixed together with about 5 wt.% CaO, a hygroscopic compound. In the former case, the amount of adsorbed water onto the starting material can be estimated by weight loss through heating at 383 K and was found to reach ca. 1 wt.%. These hydration conditions are referred to as *intermediate* hereafter. Gasc et al. (2011) showed, using in-situ impedance spectroscopy on an $Mg(OH)_2$ aggregate at 2 GPa, that in a similar set-up where the sample is only partly sealed, such absorbed water mostly remains in the sample for several hours at temperature below ca. 980 K. In the case where CaO (lime) was added to the oven-dried sample powder, residual free-water from the sample and its close environment was removed below the set-point temperature by chemical drying following the reaction:

172

173 $$CaO + H_2O \rightarrow Ca(OH)_2 \quad (2)$$

174

175 This method has been successfully used in Gasc et al. (2011), who showed progressive sample drying,
176 through CaO hydroxylation, as evidenced by a drop of the sample bulk electrical conductivity upon heating
177 at temperatures as low 673 K. Lime hydroxylation was similarly evidenced here by the pronounced
178 decrease of the CaO reflections intensity upon heating at T > 500 K, i.e., while the reaction of interest (1)
179 had not yet started (Figure 1). As long as CaO and $Ca(OH)_2$ are present in the sample, the starting water
180 activity is buffered to a value that depends on the free enthalpy of Reaction (2) and therefore on
181 temperature. The water activity was calculated using Wintwq 2.34 (Berman & Aranovich, 1996) in the
182 823–873 K temperature range corresponding to our experiments and was found to vary from 0.1 to 0.15.
183 These experiments, which involve chemical drying, will be called *dry* in the following.

184 A white x-ray beam provided by the DORIS III storage ring was used to collect energy dispersive
185 XRPD data. The spectra were collected continuously with acquisition times of 45 or 60 seconds (Figures 1
186 and 2) with a 2048 channels solid-state Ge detector. The Bragg reflection of highest intensity typically
187 varied from 2×10^3 to 5×10^3 detector counts.

188 Reaction progress, $\xi(t)$, was calculated for each spectrum collected at a time, t, from the intensity,
189 $I(t)$ of selected diffraction peaks, assuming that $\xi(t) = I(t)/I_{max}$ for products and that $\xi(t) = 1-(I(t)/I_{max})$ for
190 reactants, where I_{max} is the maximum intensity of the considered reflection (Lathe *et al.*, 2005, Zinn *et al.*,
191 1995). Therefore, for reactants, at $t = 0$, $\xi(t) = 0$ and $I(0) = I_{max}$. We calculated reaction progress either from
192 the intensity of the (104) reflection of $MgCO_3$ or the (011) reflection of $Ca(OH)_2$ (Figure 2). Because of its
193 larger grain size distribution, magnesite is less suitable for quantification purposes using X-ray powder
194 diffraction than portlandite, which was thus preferentially used to calculate $\xi(t)$. Note that, with the use
195 of white synchrotron light, the beam is collimated and the volume sampled is relatively small, which, in
196 some cases, may translate as an insufficient number of grains sampled for proper quantitative analysis.
197 This can cause the relative intensities of the diffraction peaks to fluctuate and not represent the actual
198 phase proportions. Therefore, whenever possible, reaction progress was additionally retrieved from the
199 (111) and (011) reflection intensities of $CaCO_3$ and $Mg(OH)_2$, respectively. In all cases, intensities, I, were
200 also subtracted a background that was estimated for each t. The ratio between maximum peak intensity
201 and background level was typically ~30. In some instances, after collection of kinetic data at a certain

constant temperature, the experiment was terminated by increasing further the temperature until $\xi(t) = 1$ was achieved, which allows retrieving I_{max} values for the reaction products and enables their use for calculating $\xi(t)$. In addition, the incident beam intensity decayed with time due to the decrease of the storage ring current. In order to account for this effect on peak intensities, and since the irradiated sample zone relative to the x-ray detector remains unchanged during an experiment, the peak intensities were normalized to the BN (100) reflection (Figure 2).

Reaction kinetics with excess water

The kinetics of the reaction was also investigated at lower temperatures by performing off-beam PC experiments, for which both longer run durations and excess water (i.e., water saturated) conditions could be more easily achieved. For these experiments, the solid starting material was loaded together with 10 wt.% deionized water in a gold capsule welded shut. This type of hydration conditions will be referred to as *saturated* hereafter. Low-friction NaCl-based pressure cells (1/2 inch) were used. More details on the pressure assembly can be found in Brunet et al. (2003). The temperature was measured with an S-type thermocouple and regulated within 1 K with a Eurotherm™ controller.

Angle dispersive XRPD patterns were collected on quenched products with a Rigaku diffractometer (Ultrax18hf-RINT2500) equipped with a Cu rotating anode (300 mA, 40 kV). XRPD data were collected using 0.02° steps at a speed of 2°/min. In this case, the reaction extent, $\xi(t)$, could be determined from reactant/product molar proportions in the quenched samples as follows. First, phase proportions were calculated using the following relation:

$$\frac{\chi_P}{\chi_B} = \varphi \frac{I_P}{I_B} \quad (3),$$

where φ is a constant, χ is the weight fraction of a given phase in the sample, I is the height (i.e., counts) of a selected diffraction peak, and the subscripts P and B stand for portlandite and brucite, respectively. The value of φ was calibrated from mixtures of known portlandite to brucite weight proportions using the height of the (001) reflection of each phase. The reaction progress, $\xi(t)$, corresponding to the molar fraction of the forming phase, brucite, was then estimated from the relation:

$$\frac{\xi}{1-\xi} = \frac{\chi_B M_B}{\chi_P M_P} \quad (4),$$

where M_P and M_B are the molar masses of portlandite and brucite, respectively.

One-dimension diffusion experiments under *intermediate* hydration level

The kinetics of Reaction (1) was further investigated in a one-dimension set-up using the piston-cylinder apparatus (1D-PC experiments) by measuring the width of the reaction zone, which developed at the interface between magnesite and portlandite polycrystals. This set-up aimed at characterizing grain-boundary transport with the simplest geometry. Contrary to the kinetic experiments described in the previous section, individual magnesite and portlandite powders (same material as for DIA and PC experiments but unmixed) were loaded one after the other in a gold capsule. As much as possible, the contact between these two materials was made planar (Figure 5a). No water was added to the capsule nor was the sample dried beforehand. The hydration level can therefore be considered here as *intermediate*. As for multi-anvil experiments, the run products of 1D-PC experiments were embedded in epoxy, cut and hand polished with diamond paste. After carbon coating, these samples were also characterized using the FE-SEM.

In order to investigate the temperature dependency of the chemical transport kinetics, these experiments were performed in the 773–873 K temperature range. Typical reaction front widths of ~ 1 mm were obtained for durations of a several days.

EXPERIMENTAL RESULTS

Bulk kinetic data from time-resolved XRD

In total, 16 experiments have been successfully performed on Reaction (1) with time-resolved in-situ XRPD at 1.8 GPa and for temperatures ranging from 573 to 873 K (Table 2). It must be noted that each dataset is composed of tens to hundreds of diffraction patterns, each represented by a data point in left and middle panels of Figure 3. Water saturated conditions were investigated at two single temperatures (393 and 423 K) through four and five PC experiments (Figure 3), respectively, which therefore correspond

to two kinetic data points for *saturated* conditions in Figure 4. Hundreds of PC experiments would have been required to achieve a time resolution on the reaction progress similar to that of the synchrotron-based experiments, which clearly emphasizes the advantage of using an in-situ technique for kinetic purposes.

The scattering observed in the kinetic data obtained from synchrotron XRPD indicates a precision of +/- 10% on the reaction progress (Figure 3). However, the precision on the reaction kinetics is better owing to the averaging of the large number of data at each PT conditions. For PC experiments, the precision on the determination of the reaction progress is expected to be better than 5 %; in particular, sample heterogeneity is averaged out by x-ray diffraction pattern collected on a larger sample volume

As one can observe from the shape of the reaction curves, the reaction rate is the fastest when the reaction starts and slows down as the reaction proceeds. Heterogeneous reactions, such as the one studied here, do not generally comply with simple kinetic laws such as zero- or first-order. Furthermore, the presence of a grain size distribution instead of single grain size in the starting material will influence the shape of the kinetic curve if the reaction process is dependent on the reactive-surface area of the reactants. Finally, change of hydration conditions from one set of experiments to another may lead to a change in the reaction process (e.g., dissolution – crystallization in the water saturated case). The overall shape of the kinetic curves can be successfully fitted to an empirical Avrami law (Avrami, 1939) with an exponent value of 0.4, which, according to Christian (1975), would reflect a diffusion limited reaction process. However, due to the truly empirical character of these fits, following (Brown *et al.*, 1962), we decided to merely compare half-reaction times (i.e., the time needed to reach $\xi = 0.5$) between all datasets in order to grasp the effect of water as a whole on the reaction kinetics (Table 2, Figure 4). Note that for the particular case of the PC experiments performed with 10 wt.% water (*water saturated* conditions), dissolution-precipitation process is expected to occur. However, aqueous species transport rate – rather than dissolution rate – may well be the rate limiting process. Diffusivity of aqueous species in bulk water is not within the scope of the present study. These “saturated” experiments should be seen as representative of the water-excess experiments usually carried out in experimental petrology.

Both series of experiments performed under *dry* and *intermediate* conditions seem to display an Arrhenius-type behavior (i.e., the logarithm of half reaction times have a linear dependency to reciprocal temperature) although, comparatively, experimental data obtained for an *intermediate* hydration level are much more scattered (Figure 4). The dependency of the reaction kinetic with water content is likely causing the important scattering observed in the *intermediate* dataset (see Discussion section). The

present results illustrate a drastic effect of water content on the kinetics. We note that similar half reaction times (ca. 1 hour) were obtained at ~823, 648 and 423 K, for *dry*, *intermediate* and *saturated* conditions, respectively, although the gap between *intermediate* and *dry* conditions seems to shrink towards higher temperatures due to an apparently larger activation energy of the kinetic under *dry* conditions.

Chemical transport through the $CaCO_3$ + $Mg(OH)_2$ reaction rims

FE-SEM images of the recovered 1D-PC samples show mineral intergrowth in reaction zones composed of $Mg(OH)_2$ and $CaCO_3$ (Figure 5a). Energy dispersive spectrometry data collected with the FE-SEM indicated that the Ca/Ca+Mg molar ratio remains constant and equal to 0.5 across the reaction zones. In all of the DIA samples, partly reacted magnesite grains are surrounded by reaction rims (Figure 5b) within which the grain size of the reaction products is found to gradually increase from the Ara+Bru | Mag to the Port | Ara+Bru interfaces. These reaction rims are composed of equimolar $Mg(OH)_2$ (brucite) + $CaCO_3$ (aragonite) and show the same textural characteristics (grain size distribution, symplectite intergrowth) as the reaction fronts in 1D-PC experiments. For 1D-PC and DIA experiments, the grain size of the reaction products varies between 30 nm and a few µm (Figure 5d and 5e), depending on temperature, water content and run duration. The constant stoichiometry (CaO/H_2O = MgO/CO_2 = 1) throughout the reaction zones in both 1-D experiments and DIA samples, implies the equality of Ca (CaO) and H (H_2O) fluxes through the Port | Ara+Bru interface. Similarly, the Mg (MgO) and C (CO_2) fluxes must be identical through the Ara+Bru | Mag interface. In experiment PC_180, a Pt chip was positioned at the interface between portlandite and magnesite. The Pt chip (Figure 5a) remained at the Port | Ara+Bru interface in the course of the diffusion process. Its presence at the interface appears to have hindered the transport of species from the Port | Ara+Bru interface to the Ara+Bru | Mag interface, as indicated by the depression of the reaction front opposite to the Pt chip. Therefore, CaO and H_2O are the mobile species in the system, whereas MgO and CO_2 remained comparatively immobile. This conclusion is in line with the grain size gradient observed across the reaction zones, where grains situated next to the Port | Ara+Bru interface formed first and are therefore larger.

$\overline{D}_{CaO}$ retrieval from 1D experiments

We showed in the previous section that the reaction zone growth in 1D-PC and DIA samples is controlled (i.e., limited) by the diffusion of CaO, assuming that H_2O diffusion is not limiting. The growth rate of the reaction zone (front or rim) depends on the molar flux of the limiting diffusing species, i.e., J_{CaO} in the present case, perpendicular to the reaction zone. Let us consider the equimolar mix of brucite and aragonite as a single phase having an effective molar volume corresponding to V_r (Figure 6a). In the planar geometry of our 1D-PC experiments, since each mole of CaO diffusing through the front results in the creation of one mole of said hypothetical phase, the growth rate of the reaction front thickness, ΔX, can be written:

$$\frac{d\Delta x}{dt} = J_{\mathrm{CaO}} V_r \quad (5),$$

According to the formalism developed by Fisler and Mackwell (1994), the first Fick's law for diffusion can be used to write the CaO flux across the reaction zone, J_{CaO}, as a function of the CaO chemical potential gradient, $d\mu_{\mathrm{CaO}}/dx$, as follows:

$$J_{\mathrm{CaO}} = -\frac{D_{\mathrm{CaO}} C_{\mathrm{CaO}}}{RT} \frac{d\mu_{\mathrm{CaO}}}{dx} \quad (6).$$

Fisler and Mackwel (1994) also showed that this latter expression can be integrated using the mean-value theorem, introducing the mean diffusion coefficient, $\bar{D}_{\mathrm{CaO}}$, which represents the mean value for the diffusion across the reaction front or rim. The flux can then be written:

$$J_{\mathrm{CaO}} = -\frac{\bar{D}_{\mathrm{CaO}} C_{\mathrm{CaO}}}{RT} \frac{\Delta\mu_{\mathrm{CaO}}}{\Delta x} \quad (7),$$

where $\Delta\mu_{\mathrm{CaO}} = \mu'_{\mathrm{CaO}} - \mu^0_{\mathrm{CaO}}$ and therefore represents the chemical potential difference across the reaction zone.

Let us now consider the Ara+Bru | Mag interface, where, by definition, $x = \Delta x$ (Figure 6a). If we consider the equilibrium between $MgCO_3$, the reaction products and the diffusing components, CaO and H_2O, we can write that:

$$\mu_{\mathrm{MgCO_3}} + \mu'_{\mathrm{CaO}} + \mu'_{\mathrm{H_2O}} = \mu_{\mathrm{Mg(OH)_2}} + \mu_{\mathrm{CaCO_3}} \quad (8).$$

In addition, at $x = 0$, $\mu^0_{CaO} = \mu_{\mathrm{Ca(OH)_2}} - \mu^0_{\mathrm{H_2O}}$. Assuming that water activity is constant across the whole sample (due to supposedly faster diffusion kinetics), then $\mu^0_{\mathrm{H_2O}} = \mu'_{\mathrm{H_2O}}$.We can therefore write:

$$\mu'_{\mathrm{H_2O}} = \mu_{\mathrm{Ca(OH)_2}} - \mu^0_{\mathrm{CaO}} \quad (9).$$

Finally, combining equations (8) and (9) gives:

$$\mu'_{\mathrm{CaO}} - \mu^0_{\mathrm{CaO}} = \mu_{\mathrm{Mg(OH)_2}} + \mu_{\mathrm{CaCO_3}} - \mu_{\mathrm{MgCO_3}} - \mu_{\mathrm{Ca(OH)_2}} \quad (10),$$

from which we find that $\Delta\mu_{\mathrm{CaO}} = \Delta_R G$. In addition, it can be noticed that, in the present case $C_{\mathrm{CaO}}.V_r = 1$. The combination of (5) and (7) then yields:

$$\frac{d\Delta x}{dt} = -\frac{\bar{D}_{\mathrm{CaO}}}{RT}\frac{\Delta_R G}{\Delta x} \quad (11).$$

We note here that the mean diffusion coefficient, $\bar{D}_{\mathrm{CaO}}$, is an effective (i.e., apparent) diffusion coefficient, considering the brucite + aragonite aggregate in the reaction zone as a homogeneous diffusing medium. Effective and grain boundary diffusion coefficients are related to one another by a ratio that depicts the shape and the volume fraction of grain boundaries available for intergranular diffusion. For example, in the ideal case where grain boundaries are planar (i.e., devoid of tortuosity) and parallel to the diffusion flux, the following relation applies (Brady, 1983):

$$\overline{D}^{GB} = \overline{D}\frac{2l}{\pi\delta} \quad (12),$$

where l is the distance separating the diffusion planes, i.e., the grain size (Figure 6a), and δ is the grain boundary width. Since this latter parameter is virtually impossible to determine, most authors choose to report the product of the grain boundary diffusivity $\overline{D}^{GB}$ and the grain boundary width, δ. However, during the diffusion process and the growth of reaction rims or fronts, l is not constant but obeys an exponential grain growth law (Joesten, 1991):

$$l = (\rho t)^{1/n} \quad (13),$$

where ρ and n are the grain coarsening rate constant and exponent, respectively. Combining relations (12) and (13) yields the expression:

$$\overline{D}^{GB} = \overline{D}\frac{2(\rho t)^{1/n}}{\pi\delta} \quad (14).$$

It has been shown indeed that the growth of reaction fronts limited by grain boundary diffusion is no more proportional to the square root of time, but that it slows down further with time due to grain coarsening, and therefore decreasing availability of grain boundaries (Gardes & Heinrich, 2011). In that case, Δx is proportional to $(t^{1-1/n})^{1/2}$, where n is the grain coarsening exponent. Here, the combination of Equations (11) and (14) gives the relation between rim thickness and time as a function of the grain boundary diffusion coefficient:

$$\frac{d\Delta x}{dt}\Delta x = -\overline{D}^{GB}\delta\frac{\Delta_R G}{RT}\frac{\pi}{2\rho^{\frac{1}{n}}}t^{-(\frac{1}{n})} \quad (15).$$

Integrating the above equation, noting that for t = 0 then Δx = 0, we obtain the relation:

$$\Delta x = \sqrt{\left(-\overline{D}^{GB}\delta\frac{\Delta_R G}{RT}\frac{\pi}{\rho^{\frac{1}{n}}}\left(\frac{n}{n-1}\right)\right)t^{\frac{n-1}{2n}}} \quad (16).$$

In the present case (see Appendix 1), the grain size of the reaction products was analyzed using SEM imaging to constrain the grain coarsening parameters, ρ and n. Relation (16) was then used to derive $\overline{D}^{GB}\delta$ from 1D-PC experiments (Table 2), where a planar geometry applies (Figure 6a).

Generally speaking, the presence of water may impact $\overline{D}_{\mathrm{CaO}}$ values by affecting any of the other parameters included in Equation (14), namely CaO mobility in the intergranular medium (i.e., $\overline{D}^{GB}_{\mathrm{CaO}}$), grain boundary width and grain growth. This holds for experimentally grown coronae and for natural metamorphic reactions as well and since these latter parameters are difficult to estimate, one might also want to compare effective diffusivity values, $\overline{D}_{\mathrm{CaO}}$. This approach was chosen by Carlson (2010), where Al effective diffusion coefficients were retrieved in the case of natural metamorphic coronae; it allows evaluating the overall effects of water content variations on the growth of reaction zones and visualizing how they affect metamorphic reaction kinetics in general.

$\overline{D}_{CaO}$ retrieval from reaction coronae (spherical setting)

Similar to our 1D-PC experiments, SEM examination of the DIA samples evidenced that the reaction proceeds via the development of reaction rims around magnesite grains. This is nicely illustrated by the coronae observed around coarser residual magnesite grains in some samples (Figure 5b). The dimensions of these reaction rims can be used to calculate effective diffusion coefficients according to the model shown in Figure 6b. We note however that, in the initial setting (at t = 0), magnesite grains are not surrounded strictly by portlandite only, but rather by a mix of finer magnesite grains and portlandite. This may result in low Ca availability for diffusion and growth of the reaction rims, which, in turn, implies that the diffusion values retrieved may be underestimated. Unfortunately, it is impossible to measure the impact of this bias on the values retrieved.

The spherical setting implies that Equations (5) through (7) defined above in a planar setting no longer apply. We used the analytical solution given for a spherical geometry in Abart et al. (2009) that relates the rim dimensions and the bulk diffusion coefficient. This relation was modified in order to take grain coarsening for *intermediate* conditions into account; the *dry* case was treated assuming constant grain size in the rim (see next section and Appendix 1 for details).

It should be noted that rim widths are determined from SEM images of sample sections which do not necessarily pass through the center of the imaged magnesite grains. This can introduce a measurement bias with apparently larger r_A/r_B ratios. Therefore, as much as possible, only rims with the lowest r_A/r_B ratio were used for the present determination (i.e., largest residual grains were preferentially picked). Additional errors may arise from the estimation of the inner and outer rim dimensions, r_B and r_A respectively (see Table 2). Errors on those measurements are of 0.1-0.3 µm (Table 2). According to Equation (A5), $\overline{D}_{\mathrm{CaO}}^{GB}\delta$ is proportional to the square of r_B/r_0., which is accounted for by the error bars in the Arrhenius plot (Figure 7a).

Diffusivity values obtained for both 1D-PC and DIA (3D) experiments are listed in Table 2 and are reported in Figure 7a (empty symbols). We note that the *intermediate* data, retrieved from 1D-PC, and DIA experiments, although conducted over very different time scales, (i.e., a few hours and several days respectively) show a good consistency. Despite the uncertainties discussed above, the results clearly show a gap between *dry* and *intermediate* conditions, where comparable diffusivities are found at 823 and 673 K, respectively.

Numerical extraction of diffusivity values from bulk reaction kinetics

The bulk reaction progress, $\xi(t)$, represents the molar fraction of magnesite (or portlandite) having reacted after a given run duration. At the scale of a single magnesite grain surrounded by portlandite, the reaction progress, $X(t)$, is related to the inner rim radius, r_b, as follows:

$$X(t) = 1 - \frac{{r_B}^3}{{r_0}^3} = 1 - y^3 \tag{17}$$

If reaction rim growth is the limiting factor to the bulk reaction progress, then reaction kinetics derived from in-situ diffraction should correspond to the magnesite rim growth kinetics (i.e., $X(t) = \xi(t)$). However, the relation between $\xi(t)$ and $X(t)$ depends on the magnesite grain size distribution. SEM images show that this distribution consists of a fine-grained fraction (<1 µm) along with coarser grains, which size can be as large as several tens of microns. We assumed a log-normal grain size distribution, typical of ground powders (Astrom, 2006, German, 2009, Sanchidrian *et al.*, 2012), characterized by γ_0 and σ, which represent respectively the mean and the standard deviation of the grain size natural logarithm. The grain size distribution was binned into 25 grain sizes with corresponding proportions (p_i). Using, again, the analytical solution derived from Abart et al. (2009) in Equation (A5), we could simulate reaction progress data, $X_i(t)$, for each grain size. Then kinetic curves (i.e., $\xi(t)$), were obtained by calculating the weighted sum: $\sum_{i=1}^{25} p_i\, X_i(t)$ with $\sum_{i=1}^{25} p_i = 1$. For each experimental data set, this approach was used to simulate kinetic data with varying values of $\overline{D}_{\mathrm{CaO}}^{GB}\delta$. The best fit to the experimental data was then obtained using a standard grid search algorithm and by minimizing the absolute value of the difference between modeled and observed kinetic curves; this method is also known as Least Absolute Deviations (LAD) method. The uncertainty on $\overline{D}_{\mathrm{CaO}}^{GB}\delta$ introduced by possible error on the initial grain size distribution is addressed in Appendix 2. It should be noted here, that, as mentioned in the experimental section of the present study, the diffraction peak intensities used to calculate reaction progress may not reflect the actual proportion of a phase in the sample at a given time but may differ significantly. Based on observations of the standard deviation in our DIA datasets, we inferred that this bias could result in errors of +/- 0.05 on $\xi(t)$, which impacts the values of $\overline{D}_{\mathrm{CaO}}^{GB}\delta$ retrieved by a factor of 3 at most.

All 10 DIA experiments under *intermediate* conditions were used to estimate the mean grain boundary diffusivity, $\overline{D}_{\mathrm{CaO}}^{GB}\delta$, in this fashion. However, for some experiments performed under *dry* conditions, the model failed to fit the experimental data satisfactorily. This can be explained by the minor amount of grain growth involved in *dry* conditions (maximum grain sizes in the reaction rims are typically no larger than tens of nanometers), which is therefore difficult to characterize (see appendix 1). Alternatively, we chose to fit the *dry* datasets without integrated grain growth, i.e., by using the analytical solution given in Abart et al. (2009), which allowed us to retrieve mean bulk diffusivity values, $\overline{D}_{\mathrm{CaO}}$. Values of grain boundary diffusion, $\overline{D}_{\mathrm{CaO}}^{GB}\delta$, were then calculated using equation (12) and an estimated grain size of l = 120 nm, based on measurements made on two recovered samples (see Appendix 1). The results are listed in Table 2 and, as a test of consistency between the bulk and the microscopic datasets, both are reported on an Arrhenius plot in Figure 7a, along with $\overline{D}_{\mathrm{CaO}}^{GB}\delta$ values from the literature (Figure 7b). Test

analysis of the retrieved diffusion values with varying grain growth parameters, *n* and *ρ*, showed that the errors introduced by the estimation of these parameters are negligible compared to other sources of errors (namely the initial grain size distribution and the experimentally determined reaction progress).

For four experiments performed under *intermediate* conditions and two experiments performed under *dry* conditions, diffusivities could be retrieved from both the microscopic approach and by simulating kinetic curves (bulk approach). The largest difference observed between the two approaches is of 1.33 log units. Although these differences seem significant at first sight, they are within the uncertainties discussed above. In fact, the two datasets evidence a good consistency between the microscopic (reaction rim and 1D diffusion fronts) and the macroscopic approaches, as highlighted by the Arrhenius plot on Figure 7a.

A drastic difference is observed between *dry* and *intermediate* datasets, where similar values of $\overline{D}^{GB}_{\mathrm{CaO}}\delta$ are found at ~823 and 673 K, respectively, similar to the temperature gap observed when comparing bulk reaction kinetics, i.e., half-reaction times (Figure 4). As for half-reaction times, the diffusivity gap between *dry* and *intermediate* seems to shrink towards higher temperatures. The activation energy returned by the Arrhenius fit in the *dry* case is 573 $\pm$ 208 kJ.mol^{-1}, which is indeed considerably larger than for the *intermediate* case (291 $\pm$ 29 kJ.mol^{-1}). But, in the former case, due to the narrower temperature range investigated, the uncertainty returned is too large to allow any assertion regarding its absolute value. Conclusively, although our results strongly suggest a larger activation energy in the *dry* case, they do not entirely exclude the possibility that the activation energy be the same in both cases (i.e., around 300 kJ.mol^{-1}).

DISCUSSION

Consistency between bulk and microscopic approaches

In order to investigate the effect of water on the $MgCO_3 + Ca(OH)_2 \rightarrow Mg(OH)_2 + CaCO_3$ reaction at 1.8 GPa, we designed experiments where the starting material is composed of a grain size distribution of the first reactant (i.e., magnesite with a log-normal distribution which includes grains > 10 µm) reacting with a fine and homogeneous matrix of the second reactant (portlandite $\leq$ 1 µm). We show here that this starting material is suitable for the estimation of mean diffusion coefficients from time-resolved in-situ XRPD provided (1) that significant reaction extents be achieved with sufficient XRD sensitivity, (2) that the

grain-size distribution of the reactants can be approximated and (3) that the texture of the reacted samples can be characterized post-mortem. Obviously, the conventional approach, which consists in measuring the growth rate of reaction rims remains more accurate for the determination of diffusion coefficients. However, the in-situ approach can be appealing in some instances since it allows fast collection of large datasets as required when investigating a range of hydration levels (or a range of pressures) at various temperatures. One obvious limitation of our in-situ approach with respect to the effect of hydration on reaction kinetics is the absence of a sealed container in order to ensure constant water concentration over the whole run duration. For example, in the case of the present brucite-bearing system at 1.8 GPa, this limitation implies that the reaction kinetics of samples containing a few thousands of ppm water cannot be reasonably investigated at temperature above ca. 950 K at the hour timescale (Gasc et al., 2011). The noble metal often used as container material strongly absorbs the x-ray radiation and therefore alters the XRD signal intensity. The use of titanium as capsule material (Chollet *et al.*, 2009) for synchrotron diffraction experiments dealing with water-bearing systems clearly opens the way to the collection of in-situ XRD data under controlled and constant water content.

Role of the geometry of the intergranular medium

It is important to note that, in the present diffusion dataset, the effect of water content is potentially twofold. Water content will modify the chemistry of the intergranular medium and impact the effective intergranular diffusivity (here $\overline{D}_{\mathrm{CaO}}^{GB}$). The presence of water can also modify the geometry of the diffusion paths through grain growth or by controlling the grain boundary width. The impact of grain coarsening on kinetics via the reduction of the intergranular medium available for diffusion can be of several orders of magnitude (Carlson & Gordon, 2004). Therefore, the effect of grain growth has been taken into account by introducing a grain-growth rate law (Appendix 1). However, it can be argued that the diffusivity gap between *dry* and *intermediate* conditions results from variations of the effective grain boundary width, δ. According to Relation (14), identical Ca diffusivity would imply that $\delta$is at least 2 orders of magnitude greater in *intermediate* than in *dry* conditions at 823 K. This seems huge in comparison to what we know about grain boundary width at ambient pressure. Although the effective grain boundary width may be larger than the structural grain boundary width, even in the absence of fluids (Marquardt *et al.*, 2011), in our *dry* conditions, the effective boundary width –which is the one of anhydrous aggregates– should not exceed significantly the structural boundary width, generally described as being equal to a few nanometers (Bons *et al.*, 1990, Farver *et al.*, 1994, Hiraga *et al.*, 1999, Ricoult & Kohlstedt,

1983, (Marquardt *et al.*, 2011). On the other hand, studies of water-mineral interface structures show that no more than two monolayers of water are adsorbed at the surface of calcite grains with water being structured over a distance of approximately 15 Å (Cooke *et al.*, 2010, Fenter & Sturchio, 2004). This implies that δ cannot vary by more than one order magnitude between *dry* and *intermediate* conditions. Conclusively, even if intergranular diffusion may be enhanced by small amounts of water through grain boundary widening, this effect alone cannot be responsible for the tremendous differences observed between *dry* and *intermediate* cases, which are greater than two orders of magnitude at the lowest temperatures of the present study (Figure 7a). As suggested by the change in activation energy from *intermediate* to *dry* condition, we are likely documenting here water-content dependent diffusion mechanisms, where cation mobility is enhanced by the presence of absorbed water at the grain surfaces (i.e., in the grain boundaries). However, it is possible that even minor amounts of water, such as it is the case here, enhance diffusivity not by widening grain boundaries – therefore increasing the structural grain boundary width – but by creating locally connected porosity (most likely in the form of tubules at triple junctions). This would result in an increased effective grain boundary width, which no longer relates to the actual structural grain boundary width; and the term intergranular diffusion should be preferred over grain boundary diffusion.

We note, however, that so far, there has been no systematic measurement of the grain boundary width or structure evolution with increasing pressure. There is, therefore, a clear need for in-situ experiments which investigate, for instance, how confining pressure affects transport properties.

Water content and intergranular Ca-diffusion regimes

The effect of water content on calcium transport (reaction rim growth) derived here is very consistent, at least from a qualitative point of view, with recent work on Mg and Al intergranular transport (Milke et al., 2013; Gardés *et al.*, 2012; Carlson, 2010). In these studies, as in the present one, the addition of small amounts of water, ≤ 1 wt.%, was reported to enhance intergranular diffusion by several orders of magnitude, resulting in equal transport properties at temperatures lower by hundreds of degrees. We note that in all cases the activation energies are reported to decrease significantly with increasing water content. The present results are also in good agreement with the results of Gasc et al. (2011), where, using a PC set-up that was open with respect to water, a drastic reduction of the electrical conductivity of polycrystalline brucite was observed between samples dried in an oven at 393 K –possibly containing adsorbed water– and samples chemically dried by the addition of CaO. This was also accompanied by an

574 increase of the activation energy of the electrical conductivity from 84 to 106 kJ mol^{-1}. Similarly, the
575 kinetics of the $Ca(OH)_2 + MgCO_3 \rightarrow CaCO_3 + Mg(OH)_2$ exchange reaction, which is also controlled by
576 intergranular transport under the investigated PT conditions, showed a strong positive dependency with
577 water content from *dry* to *saturated* conditions (Figure 4).

578 In the present study, *dry* conditions were achieved using chemical drying, i.e., by maintaining low
579 water fugacity in the sample with a $CaO/Ca(OH)_2$ solid buffer. The notion of *dry* conditions may appear
580 somehow contradictory since the *dry* sample contains hydroxide phases. It should rather be understood
581 in the frame of diffusivity regimes (Farver & Yund, 1995), which were recently redefined by Gardés et al.
582 (2012) on enstatite and enstatite + forsterite reaction rims. These authors suggested that four different
583 regimes can be distinguished as a function of water content; the first regime corresponding to conditions
584 where grain boundaries are essentially anhydrous. The exchange of water between brucite inner grains
585 and grain boundaries observed by Gasc et al. (2011) precludes the occurrence of anhydrous grain
586 boundaries in the presence of brucite, as in the present study. Indeed, Milke et al. (2013) showed that
587 water content at the 10^{th} of ppm level is sufficient to switch from anhydrous to hydrous-like reaction
588 textures in OPX reaction rims at 850-900°C. Hence, the *dry* conditions obtained here with the addition of
589 CaO cannot correspond to Regime 1 defined by Gardés et al. (2012). In addition, the fact that our diffusion
590 data show the least scattering in the *dry* case (Figures 4 and 7a) suggests that they are relevant to Regime
591 3, corresponding to hydrous saturated grain boundary, rather than Regime 2 where diffusivity is expected
592 to be strongly dependent of water content. Regarding our *intermediate* conditions, although our approach
593 suffers from undetermined water content, the absorbed water on grain surfaces is estimated to represent
594 1 wt.% of the starting material at most, a value that is close to the 0.5 wt.% threshold proposed by Gardés
595 et al. (2012) for the transition between Regimes 3 and 4 for anhydrous magnesium silicates. Besides,
596 according to Gardés et al. (2012), diffusivity variations with water content are also expected to be
597 encountered in Regime 4, where interconnected fluid channels start occurring. This is consistent with the
598 scattering of our diffusivity data in *intermediate* conditions, since the water content in the sample likely
599 varied from one experiment to the other due to variable hygrometric conditions and to partial water
600 draining during the experiment. In fact, it might not be fortuitous that the lowest temperature datapoint
601 at 573 K performed under *intermediate* conditions led to a significantly higher diffusivity value than its
602 counterparts. For this reason, and despite the low uncertainty returned, the (apparent) activation energy
603 for the *intermediate* conditions should be considered with caution.

Helpa et al. (2014) studied experimentally Mg and Ca diffusion in dolomite reaction rims but could not distinguish whether GB or volume diffusion was the dominant process. Both studies were performed in anhydrous conditions and their results are compared to ours in Figure 7b. Extrapolation of the Ca diffusion coefficients obtained in *dry* conditions to the 750-800°C temperature range indicates that we found higher diffusivity by four and six orders of magnitude than Helpa et al. (2014) and Farver and Jund (1996), respectively. This apparent discrepancy can be accounted for by different water conditions investigated by these authors, which likely corresponded to Regime 1 (anhydrous) whereas we interpreted our *dry* experiments as reflecting diffusional Regime 3 defined by Gardés et al. (2012). For comparison, we also plotted on Figure 7b, the data on Mg diffusion in enstatite rims by Gardés et al. (2012) and Gardés and Heinrich (2011) who respectively investigated Regime 3 and Regime 1. It can be seen that differences of, at least, 6 orders of magnitude are encountered at 800°C between these two diffusional regimes for $\overline{D}_{MgO}^{GB}\delta$. This comparison with Mg diffusivity in enstatite rims confirms that our *dry* conditions are consistent with Regime 3.

Interestingly, a major difference between our results and the ones of Helpa et al. (2014) is the unilateral aspect of the diffusion in our case, where Mg immobility is evidenced, whereas both species (Mg and Ca) are found to diffuse at comparable rates in the experiments of Helpa et al (2014). The difference is even more notable when comparing to the Mg-Ca-Si system, where it has been established that Mg is the most mobile specie (Joachim *et al.*, 2011, Joachim *et al.*, 2012). Although these differences are admittedly difficult to interpret in terms of diffusion mechanisms, it may well be related to the fact that, in our particular case, Ca diffuses jointly with H_2O, associated to the breakdown of portlandite upon reaction, which could, in turn, result in faster Ca mobility, relative to Mg.

Oxygen diffusivity in grain boundary of hot-pressed calcite aggregates was investigated by Farver and Jund (1998) under hydrous conditions (Regime 3). As shown on Figure 7b, the corresponding $D^{GB}\delta$ values for oxygen under these water conditions lie around our Ca diffusion data under *intermediate* conditions.

One of the most striking feature of Figure 7b is the location of the Mg intergranular high-temperature diffusivity data (0.1-0.5 and 5 wt.% H_2O, i.e., Regime 3 and 4, respectively) derived by Gardés et al. (2012). Despite the addition of water, these data lie on the very slow diffusion side of the plot, relatively close to the data for Ca diffusion in anhydrous carbonates (Farver and Yund, 1996; Helpa et al., 2014) and far from hydrous Ca and O diffusion data in carbonates (this study and Farver and Jund, 1996, respectively). We believe that this discrepancy does not rely on the element/oxide that is considered (Mg

635 vs. Ca/O) in these studies but rather on the mineralogical/chemical system that was investigated: silicate
636 on the one side and $CaCO_3$ (Farver and Yund, 1994, 1996), $CaMg(CO_3)_2$ (Helpa et al., 2014) or $CaCO_3$-
637 $Mg(OH)_2$ (this study) on the other side. In the case of volume diffusion, such differences were already
638 pointed out by Farver (1994), who showed that oxygen self-diffusion in non-silicates such as magnetite,
639 apatite and calcite, is more than two orders of magnitude larger than in silicates with the same total ionic
640 porosity. In the present case, it is very likely that the hydrated brucite surfaces provide a faster diffusion
641 medium than the silicate ones in Gardés et al. (2012), the hydrophobic surface of which likely favors the
642 formation of water pores even at the 10^{th} of ppm water content level (e.g., Milke et al., 2013). However,
643 in this case, one would expect their experiments performed in Regime 4, with saturated hydrous grain
644 boundaries, to yield diffusion coefficients similar or close to ours, which is far from true, as shown by the
645 data point corresponding to 1 wt.% of water from Gardés et al. (2012) in Figure 7b. One major aspect one
646 has to keep in mind when comparing these results is that, unlike for self-diffusion experiments, the
647 diffusion mechanism, here, as well as in Gardés et al. (2012), is driven by a chemical reaction, as shown
648 by the presence of the ΔG term in our Equations (16) and (A5) or in Equations (1), (2) and (3) of Gardés et
649 al. (2012). Now, the GB diffusivity contrast between our experiments and those of Gardés et al. (2012)
650 implies a huge gap between the temperatures required to achieve measurable reaction rims at laboratory
651 timescale (400°C vs. 1000°C, respectively). We believe that this highlights the generally well known
652 difference between reaction kinetics in silicate and carbonate systems, which is often expressed in terms
653 of dissolution rates contrast between rather soluble carbonates and less soluble silicates (Dolejs and
654 Manning (2010) and references therein). In nature, when intergranular fluids are present and transport is
655 no longer limiting, these solubility differences tend to control the kinetics of metamorphic equilibration
656 (Carlson *et al.*, 2015). We show here that the kinetic contrast between the silicate and carbonate systems
657 seems to hold at very low water contents and even under *dry* conditions. As a consequence, although the
658 drastic effect of low water content (< 1 wt.%) on intergranular diffusion in mineral aggregates can be
659 understood in the frame of water sensitive diffusional regimes (Rubie, 1986; Farver and Jund, 1995;
660 Carlson, 2010, Gardés et al., 2012), substantial intergranular diffusivity variations will depend on the
661 chemical and physical properties of intergranular media, which may drastically differ in laboratory
662 experiments and in Nature.

663

664 **Implications for metamorphism**

665 The need for short run duration imposed by the synchrotron beam availability led us to focus on
666 a system characterized by relatively high reaction kinetics, even under *dry* conditions. Consequently, our
667 experiments significantly departed from nature-relevant kinetics, where slow diffusing species such as Al
668 control the reaction rate. Our conclusions on the effect of water content are, however, in line with those
669 from Carlson (2010) who, based on natural metamorphic reaction coronae, showed that large gaps exist
670 between aluminum grain boundary diffusivities under "nearly anhydrous" and "hydrous but fluid-
671 undersaturated" conditions. Carlson (2010) also suggested an increase of the activation energy of the
672 diffusion from fluid-saturated to anhydrous conditions. Furthermore, it seems that another large
673 diffusivity gap exists as the water content increases and the fluid phase becomes interconnected (Brenan,
674 1993). Considering now the recent study by Gardés et al. (2012), which depicts the same type of picture,
675 it seems that a general scheme arises with a set of diffusivity regimes controlled by water content.

676 A central question with respect to natural systems is whether water content will affect
677 metamorphic reactions in the temperature range at which they occur. Indeed, the decrease of the
678 activation energy of the diffusion with increasing water content, suggests that reaction kinetics are
679 unaffected by water content above a given temperature. In our case, the temperature corresponding to
680 the intersection between the Arrhenius laws determined under *dry* and *intermediate* conditions lies at
681 ~ 1600 K. For both the data reported by Carlson (2010) and Gardés et al. (2012), this intersection is found
682 at even higher temperature values. It is therefore likely that the strong effect of water activity (even when
683 < 1) on reaction kinetics reported here will be relevant to most metamorphic conditions.

684 In high-grade lower crustal rocks, water activity is mostly expected to be below unity (e.g., Yardley
685 and Valley, 1997) and, therefore, aside from Regime 4, the various diffusivity regimes re-defined by
686 Gardés et al. (2012) can potentially operate. In dry lower-crustal rocks, when hydrous silicates are still
687 present, for example, water activity is close to 10^{-2} (Yardley and Valley, 1997), this corresponds to what
688 we called *dry* conditions here and tentatively interpreted as saturated (or partly saturated) grain
689 boundaries, although in the absence of free fluids. Even if our understanding of intergranular transport in
690 water undersaturated rock is still very poor, our experiments show that, in lower crustal rocks, grain
691 boundary diffusion rates are rendered much faster by the simple presence of hydrous phases such as
692 brucite. Furthermore, since the addition of minor amounts of water are sufficient to allow transition from
693 Regime 3 to 4, mineral reaction rates are prone to vary by several orders of magnitude with relatively
694 small changes in water activity. It can therefore be emphasized that, as much as temperature, water
695 activity is a first order parameter that will control reaction rates among minerals. In water-bearing rocks

– meaning here rocks which are not anhydrous – the effect of increasing temperature on grain boundary diffusivity will be enhanced by structural water contained in hydrous minerals being progressively transferred into grain boundaries, e.g., Gasc et al. (2011) for a laboratory case and Hetenyi et al. (2007) for a natural case.

APPENDIX 1: Estimation of grain coarsening parameters and implementation in the analytical solution of Abart et al. (2009) for a spherical geometry.

Sample PC175 which was obtained under intermediate conditions exhibits the largest reaction front, which allows the most precise characterization of grain growth among our samples. Measurements of grain size across the reaction front showed that it is proportional to the distance from the Ara+Bru | Mag interface, where the products nucleate (Figure A1).

This implies that the grain size of the products is proportional to the reaction front width, i.e. $l \propto \Delta x$. Since PC175 is a 1-D diffusion experiment, we can consider the relation defined by Gardés and Heinrich (2011) where reaction front growth controlled by grain boundary diffusion obeys:

$$\Delta x = A\sqrt{t^{1-1/n}} \quad \text{(A1)}$$

and where *A* is a constant, and *n* is the grain growth exponent. At a given temperature, grain growth is known to have an exponential dependence with time of the form

$$l = (\rho t)^{1/n} \quad \text{(A2)},$$

where *ρ* is the growth rate constant. Proportionality between grain size and $\Delta \boldsymbol{x}$ whatever *t* implies that $\frac{1-1/\mathrm{n}}{2} = 1/\mathrm{n}$ **,** i.e, *n* = 3. Note that this is the value of n that is used in Gardés and Heinrich (2011). Then, assuming a value of *n* =3 for *intermediate* conditions, *ρ* could be retrieved for experiments where SEM images allowed measuring the maximum grain size, *l*, of the products; and using Equation (A2). This was done for six *intermediate* and two *dry* conditions experiments, respectively. However, under dry conditions, grain growth is limited, with final grain sizes that never exceed 150 nm. In addition, the nucleus size of the reaction products in the reaction rim is unknown. Grain growth in *dry* conditions was therefore neglected without inducing significant error on the retrieved diffusion values.

The temperature dependency of *ρ* is of Arrhenius type:

$$\rho = \rho_0 \times exp\left[-\frac{Q}{RT}\right] \quad \text{(A3)},$$

with Q = 274 kJ mol^{-1} and r_0 = 6.85 × 10^{-5} m$^{1/3}$ s^{-1} for the *intermediate* dataset (Fig. A2). Using relation (A3), ρ could be calculated for all DIA experiments run under *intermediate* conditions and further used to calculate the corresponding $\overline{D}_{\mathrm{CaO}}^{GB}\delta$ product as described in the Results section.

In order to use the grain coarsening model above to retrieve $\overline{D}_{\mathrm{CaO}}^{GB}\delta$ in the spherical geometry, differential equation (32) *in* Abart et al. (2009) has been modified to yield the following integral form:

$$\int_1^y y\left(\frac{y}{(1+u(y^3-1))^{1/3}}-1\right)dy = -\overline{D}_{\mathrm{CaO}}^{GB}\delta\frac{\Delta_r G}{RT}\frac{V_m}{V_r}\frac{\pi}{2r_0^2\rho^{1/n}}\int_0^t t^{-\frac{1}{n}}dt \quad \text{(A4)}$$

Noting that y = 1 for t = 0, we obtain the relation between grain boundary diffusivity, time and rim dimensions for a spherical geometry:

$$\frac{1-y^2}{2}-\frac{1}{2u}\left\{1-[1+u(y^3-1)]^{2/3}\right\} = -\overline{D}_{\mathrm{CaO}}^{GB}\delta\frac{\Delta_r G}{RT}\frac{V_m}{V_r}\frac{\pi}{2r_0^2\rho^{1/n}}\frac{n}{n-1}t^{\frac{n-1}{n}} \quad \text{(A5)}$$

where $y = \frac{r_B}{r_0}$.

Equation (A5) was used to calculate grain boundary diffusion coefficients based on measurements of r_A and r_B (Figure 6b). However, using this solution implies calculating first the position of the initial interface r_0. The position of r_0 relative to r_A and r_B can be found assuming that one mole of portlandite (i.e., CaO + H_2O) entering the rim, yields one mole of reaction products, $n_M = n_r$, where, again, the brucite + aragonite assemblage is considered as a single phase with a molar volume V_r that is the sum of brucite and aragonite individual molar volumes. We note that, at any time, the volume of a magnesite grain having reacted corresponds to $n_M V_M = \frac{4}{3}\pi({r_0}^3 - {r_B}^3)$. Similarly, we can write that the volume of the reaction products corresponds to the volume of the rim, $n_p V_r = \frac{4}{3}\pi({r_A}^3 - {r_B}^3)$. As stated above, the equality between the number of moles on each side, leads to the relation:

$$\frac{V_M}{V_r} = \frac{{r_0}^3-{r_B}^3}{{r_A}^3-{r_B}^3} \quad \text{(A6)}$$

The r_0 values were therefore calculated using Equation (A6) and then used to retrieve $\overline{D}_{\mathrm{CaO}}^{GB}\delta$ values with Equation (A5).

APPENDIX 2: Dependency of diffusivity data on the input grain size distribution

The distribution of the initial magnesite grain size in our model impacts the diffusion coefficient retrieved, simply because finer grains tend to react faster than their coarser counterparts. Although the initial grain size distribution was partly characterized by SEM images, the consistency between the two parameters that control the grain size distribution, $\gamma_0$and σ, and the actual magnesite grains dimensions was tested by a series of simulations. This also allowed us to estimate the errors resulting from approximations made on the aforementioned grain size distribution.

In the log-normal distribution, γ_0 represents the natural logarithm of the median value, which, based on SEM characterization, was set to 2 µm. The impact of γ_0 on diffusivity was tested for values varying from $\exp(\gamma_0) = 1-5$ µm. In the investigated range, the retrieved $\overline{D}_{\mathrm{CaO}}^{GB}\delta$ values vary almost linearly with γ_0 (from 1.66×10^{-24} to 4.94×10^{-23} m^3s^{-1} for experiment X11, for example). The parameter σ is also critical since it impacts the proportion of large grains present in the sample; it was estimated based on SEM images, which show that large grains, coarser than 20 µm, represent ~30% of the whole magnesite initial volume. This is best modeled with σ = ln(2.5). However, we considered here that the uncertainty resulting from the error on σ corresponds to $2.2 < \exp(\sigma) < 2.9$, which translates into a volume percentage of large grains comprised between ~10 to 50 %. We remind that this error does not represent an actual variation of grain size distribution in the starting material but rather the amount of large grains sampled by the X-ray beam –therefore contributing to the overall kinetic. This may vary due to poor statistics, i.e. a handful of large grains only could result in an apparently slower kinetic, and, in the contrary, if little to no large grains are present, kinetic will appear faster, as it will be mainly controlled by the reaction of small grains. The results of these tests show that, for experiment X11 for example, when $\exp(\sigma)$ varies from 2.2 to 2.9, the obtained values of $\overline{D}_{\mathrm{CaO}}^{GB}\delta$ vary from 2.80×10^{-24} to 2.25×10^{-23} m^3s^{-1}. It should be noted here, that we expect the grain size distribution in the starting material to be similar in all experiments and, therefore, errors discussed above should not affect the variations of $\overline{D}_{\mathrm{CaO}}^{GB}\delta$ observed upon water content and temperature.

ACKNOWLEDGEMENTS

Univ. Paris-XI funded JG PhD grant. Financial support through PROCOPE (grant 09383RJ), HASYLAB and SYSTER (CNRS-INSU) is acknowledged. We are indebted to E. Gardés, W. Carlson and an anonymous reviewer for very constructive reviews that greatly improved the manuscript. The authors thank G. Hetényi, D. Daval and A. Fernandez-Martinez for valuable discussions.

FIGURE CAPTIONS

Figure 1: XRPD patterns collected on sample Y13 showing the early water activity buffering of the lime (LIM) – portlandite (POR) pair upon heating at 1.8 GPa. MAG, BRU, CAL and ARA stand for magnesite, brucite, calcite and aragonite, respectively. The grey and black patterns correspond to data collected at room temperature and shortly before the target temperature of 833 K was reached, respectively. Note that most peaks are shifted towards lower energies upon heating due to thermal expansion. At ca. 833 K upon heating, small amounts of reaction products, i.e., brucite and aragonite, are present along with minor transient calcite. The persistence of CaO is evidenced by its (200) reflection at 33.85 keV (black pattern), the intensity of which drastically decreased upon heating, as shown by the comparison between the grey and black diffraction patterns, then remained constant during the rest of the experiment. The partial consumption of CaO is interpreted as resulting from the reaction with the sample/assembly water to form $Ca(OH)_2$. Numbers in parentheses are Miller indices of the diffracting planes.

Figure 2: In-situ XRPD data for Reaction (1) under *intermediate* conditions at 573 K and 1.8 GPa (run X15). The spectra were collected with a step time of 45 s. The main diffraction peaks are indexed, including reflections used for the calculation of reaction progress and the BN reflection used for intensity normalization. Note that the corresponding diffraction energies differ from Figure 1 due to a different angle of the detector relative to the incident beam.

Figure 3: Bulk kinetic data (reaction progress) and simulated kinetic curves. (a) *Dry* conditions (DIA); (b) *Intermediate* conditions (DIA); (c) *Saturated* conditions (PC). Reaction progress data were obtained from diffraction reflections relative intensities for (a) and (b) (see text for details) and from Equation (4) for (c).

Figure 4: Half-reaction times obtained from all 16 DIA experiments as well as from the two sets of PC experiments, at 393 K and 423 K. Values are plotted on a logarithmic scale vs. reciprocal temperature. Usual time measures are given as a guide to apprehend the tremendous effect of temperature on the kinetics, which range from seconds to weeks within less than a 200-degree span. Triangles, diamonds and circles stand for *dry*, *intermediate* and water *saturated* conditions, respectively.

Figure 5: FE-SEM images in back-scattered electrons (BSE) mode of recovered samples. Abbreviations Por, Mag, Bru and Ara stand for portlandite, magnesite, brucite and aragonite respectively. (a) 1D-PC sample PC180. The reaction front between Portlandite (lower, bright phase) and $MgCO_3$ (upper dark phase) is visible. The Pt chip (white color) is at the Port | Ara+Bru interface. The fracture network formed upon sample decompression and was not present when the sample reacted. (b) and (c) DIA samples Y10 and Y11, respectively. After collection of the kinetic data (shown in Figure 3) the temperature was increased for both samples to ~1073 K (see experimental section for details). (b) As a result these samples show large reaction rims around the coarsest residual magnesite grains. (c) Also thanks to higher temperatures, nicely defined palisade-type rims with brucite and aragonite (darker and brighter phases, respectively)

intergrowths are observed. The edge of a residual magnesite grain is visible in the lower left corner. (d) and (e) Detailed views of a reaction rim in samples AA13 and AA10, respectively. The reacting magnesite grain is visible in the bottom lower corner in both cases. Note the finer grain size of the reaction products in (e), due to a lower temperature.

Figure 6: Idealized geometries taken for the calculation of $\bar{D}^{\mathrm{GB}}_{\mathrm{CaO}}\delta$. (a) Planar geometry used for calculations of diffusion coefficients from reaction front thickness (1D-PC experiments). (b) Spherical geometry used for the calculation of $\bar{D}^{GB}_{\mathrm{CaO}}\delta$ from reaction rim dimensions (DIA experiments, microscopic approach) and using the analytical solution derived from Abart et al. (2009) to fit the kinetic curves (DIA experiments, macroscopic approach).

Figure 7: Summary of the $\boldsymbol{\bar{D}^{GB}_{\mathrm{CaO}}\delta}$ values obtained in this study and comparison with literature data. (a) Triangles and squares correspond to *intermediate* and *dry* data, respectively. Empty symbols represent values retrieved from SEM measurements of reaction rim widths for both *intermediate* and *dry* conditions (microscopic approach) with down-pointing triangles representing the 1D-PC data obtained under *intermediate* conditions. Diffusion data extracted from reaction progress vs. time curves are reported with filled symbols (bulk approach). The dashed lines represent Arrhenius laws obtained by least square fitting of the *dry* and *intermediate* data; the activation energies and their respective uncertainties obtained are also labelled. (b) The Arrhenius laws corresponding to our data and shown on (a) are also reported here (same dashed lines) along with grain boundary diffusion data from the literature regarding carbonates: Farver and Yund (1996), Ca diffusion in calcite (empty diamonds); Farver and Yund (1998), O diffusion in calcite (filled diamonds); Helpa et al. (2014), Ca diffusion during dolomite rim growth (empty stars). Additional data were added to illustrate previously demonstrated effect of water content: the black and grey curves and the circle represent diffusion regimes 1, 3 and 4 of Mg in enstatite grain boundaries, as defined in Gardés and Heinrich (2011) and Gardés et al. (2012); these correspond to dry conditions and 0.1-0.5 wt.% and 2.1 wt.% water, respectively.

Figure A1: Grain size of the reaction products across the reaction front in sample PC175. Grain sizes correspond to the average measurement of the five largest identified grains in each location. An SEM backscattered electron image of the reaction front is superimposed to illustrate the grain size gradient.

Figure A2: Arrhenius plot showing the values of ρ obtained from grain size measurements at various temperatures for *intermediate* and *dry* experiments (circles and squares, respectively). The linear regression shown by the dashed line returned the values indicated in the adjacent box, according to equation (A3), with Q in J mol^{-1}.

REFERENCES

Abart, R., Petrishcheva, E., Fischer, F. D. & Svoboda, J. (2009). Thermodynamic model for diffusion controlled reaction rim growth in a binary system: application to the forsterite-enstatite-quartz system. *American Journal of Science* **309**, 114-131.

Astrom, J. A. (2006). Statistical models of brittle fragmentation. *Advances in Physics* **55**, 247-278.

Austrheim, H. (1987). Eclogitization of lower crustal granulites by fluid migration through shear zones. *Earth and Planetary Science Letters* **81**, 221-232.

Avrami, M. (1939). Kinetics of phase change I - General theory. *Journal of Chemical Physics* **7**, 1103-1112.

Baxter, E. F. (2003). Natural constraints on metamorphic reaction rates. In: Vance, D., Muller, W. & Villa, I. M. (eds.) *Geochronology: Linking the Isotopic Record with Petrology and Textures*. Bath: Geological Soc Publishing House, 183-202.

Berman, R. G. & Aranovich, L. Y. (1996). Optimized standard state and solution properties of minerals .1. Model calibration for olivine, orthpyroxene, cordierite, garnet, ilmenite in the system FEO-MGO-CaO-Al2O3-TiO3-SiO2. *Contributions to Mineralogy and Petrology* **126**, 1-24.

Bons, A. J., Drury, M. R., Schryvers, D. & Zwart, H. J. (1990). The nature of grain-boundaries in slates - implications for mass-transport processes during low-temperature metamorphism. *Physics and Chemistry of Minerals* **17**, 402-408.

Brady, J. B. (1983). Intergranular diffusion in metamorphic rocks. *American Journal of Science* **283**, 19.

Brenan, J. M. (1993). Diffusion of chlorine in fluid-bearing quartzite - effects of fluid composition and total porosity. *Contributions to Mineralogy and Petrology* **115**, 215-224.

Brown, W. H., Fyfe, W. S. & Turner, F. J. (1962). Aragonite in california glaucophane schists, and the kinetics of the aragonite-calcite transformation. *Journal of Petrology* **3**, 566-&.

Brunet, F., Bagdassarov, N. & Miletich, R. (2003). Na3Al2(PO4)(3), a fast sodium conductor at high pressure: in-situ impedance spectroscopy characterisation and phase diagram up to 8 GPa. *Solid State Ionics* **159**, 35-47.

Carlson, W. D. & Gordon, C. L. (2004). Effects of matrix grain size on the kinetics of intergranular diffusion. *Journal of Metamorphic Geology* **22**, 733-742.

Carlson, W. D. (2010). Dependence of reaction kinetics on H2O activity as inferred from rates of intergranular diffusion of aluminium. *Journal of Metamorphic Geology* **28**, 735-752.

Carlson, W. D., Hixon, J. D., Garber, J. M. & Bodnar, R. J. (2015). Controls on metamorphic equilibration: the importance of intergranular solubilities mediated by fluid composition. *Journal of Metamorphic Geology* **33**, 123-146.

Chollet, M., Daniel, I., Koga, K. T., Petitgirard, S. & Morard, G. (2009). Dehydration kinetics of talc and 10 angstrom phase: Consequences for subduction zone seismicity. *Earth and Planetary Science Letters* **284**, 57-64.

Christian, J. W. (1975). Theory of transformations in metals and alloys. I. Equilibrium and general kinetic theory, 2nd edition. *Theory of transformations in metals and alloys. I. Equilibrium and general kinetic theory, 2nd edition*, xvi+586 pp-xvi+586 pp.

902 Cooke, D. J., Gray, R. J., Sand, K. K., Stipp, S. L. S. & Elliott, J. A. (2010). Interaction of Ethanol and
903 Water with the {1014} Surface of Calcite. *Langmuir* **26**, 14520-14529.
904 Decker, D. L. (1971). High-pressure equation of state for NaCl, KCl, and CsCl. *Journal of Applied*
905 *Physics* **42**, 3239-&.
906 Dolejs, D. & Manning, C. E. (2010). Thermodynamic model for mineral solubility in aqueous fluids:
907 theory, calibration and application to model fluid-flow systems. *Geofluids* **10**, 20-40.
908 Farver, J. R. (1994). OXYGEN SELF-DIFFUSION IN CALCITE - DEPENDENCE ON
909 TEMPERATURE AND WATER FUGACITY. *Earth and Planetary Science Letters* **121**, 575-587.
910 Farver, J. R. & Yund, R. A. (1995). Grain-boundary diffusion of oxygen, potassium and calcium in
911 natural and hot-pressed feldspar aggregates. *Contributions to Mineralogy and Petrology* **118**, 340-355.
912 Farver, J. R. & Yund, R. A. (1996). Volume and grain boundary diffusion of calcium in natural and hot-
913 pressed calcite aggregates. *Contributions to Mineralogy and Petrology* **123**, 77-91.
914 Farver, J. R. & Yund, R. A. (1998). Oxygen grain boundary diffusion in natural and hot-pressed calcite
915 aggregates. *Earth and Planetary Science Letters* **161**, 189-200.
916 Farver, J. R., Yund, R. A. & Rubie, D. C. (1994). Magnesium grain-boundary diffusion in forsterite
917 aggregates at 1000-degrees-1300-degrees-C and 0.1-MPa TO 10-GPa. *Journal of Geophysical Research-*
918 *Solid Earth* **99**, 19809-19819.
919 Fenter, P. & Sturchio, N. C. (2004). Mineral-water interfacial structures revealed by synchrotron X-ray
920 scattering. *Progress in Surface Science* **77**, 171-258.
921 Fisler, D. F. & Mackwell, S. J. (1994). Kinetics of diffusion-controlled growth of fayalite. *Physics and*
922 *Chemistry of Minerals* **21**, 156-165.
923 Gardés, E. & Heinrich, W. (2011). Growth of multilayered polycrystalline reaction rims in the MgO-SiO2
924 system, part II: modelling. *Contributions to Mineralogy and Petrology* **162**, 37-49.

925 Gardés, E., Wunder, B., Marquardt, K. & Heinrich, W. (2012). The effect of water on intergranular mass
926 transport: new insights from diffusion-controlled reaction rims in the MgO-SiO2 system. *Contributions to*
927 *Mineralogy and Petrology* **164**, 1-16.
928 Gasc, J., Brunet, F., Bagdassarov, N. & Morales-Florez, V. (2011). Electrical conductivity of
929 polycrystalline Mg(OH)(2) at 2 GPa: effect of grain boundary hydration-dehydration. *Physics and*
930 *Chemistry of Minerals* **38**, 543-556.
931 German, R. M. (2009). Fragmentation behaviour in particulate materials processing. *Powder Metallurgy*
932 **52**, 196-204.
933 Helpa, V., Rybacki, E., Abart, R., Morales, L. F. G., Rhede, D., Jerabek, P. & Dresen, G. (2014).
934 Reaction kinetics of dolomite rim growth. *Contributions to Mineralogy and Petrology* **167**.

935 Hetenyi, G., Cattin, R., Brunet, F., Bollinger, L., Vergne, J., Nabelek, J. & Diament, M. (2007). Density
936 distribution of the India plate beneath the Tibetan plateau: Geophysical and petrological constraints on the
937 kinetics of lower-crustal eclogitization. *Earth and Planetary Science Letters* **264**, 226-244.
938 Hiraga, T., Nagase, T. & Akizuki, M. (1999). The structure of grain boundaries in granite-origin
939 ultramylonite studied by high-resolution electron microscopy. *Physics and Chemistry of Minerals* **26**,
940 617-623.
941 Joachim, B., Gardés, E., Abart, R. & Heinrich, W. (2011). Experimental growth of Akermanite reaction
942 rims between wollastonite and monticellite: evidence for volume diffusion control. *Contributions to*
943 *Mineralogy and Petrology* **161**, 389-399.

944 Joachim, B., Gardés, E., Velickov, B., Abart, R. & Heinrich, W. (2012). Experimental growth of diopside
945 plus merwinite reaction rims: The effect of water on microstructure development. *American Mineralogist*
946 **97**, 220-230.
947 Joesten, R. L. (1991). Kinetics of coarsening and diffusion-controlled mineral growth. *Reviews in*
948 *Mineralogy* **26**, 507-582.

949 John, T. & Schenk, V. (2003). Partial eclogitisation of gabbroic rocks in a late Precambrian subduction
950 zone (Zambia): prograde metamorphism triggered by fluid infiltration. *Contributions to Mineralogy and*
951 *Petrology* **146**, 174-191.
952 Lathe, C., Koch-Muller, M., Wirth, R., van Westrenen, W., Mueller, H. J., Schilling, F. & Lauterjung, J.
953 (2005). The influence of OH in coesite on the kinetics of the coesite-quartz phase transition. *American*
954 *Mineralogist* **90**, 36-43.
955 Marquardt, K., Ramasse, Q. M., Kisielowski, C. & Wirth, R. (2011). Diffusion in yttrium aluminium
956 garnet at the nanometer-scale: Insight into the effective grain boundary width. *American Mineralogist* **96**,
957 1521-1529.

958 Milke, R., Kolzer, K., Koch-Muller, M. & Wunder, B. (2009). Orthopyroxene rim growth between
959 olivine and quartz at low temperatures (750-950A degrees C) and low water concentration. *Mineralogy*
960 *and Petrology* **97**, 223-232.
961 Milke, R., Neusser, G., Kolzer, C., Wunder, B. (2013): Very little water is necessary to make a dry solid
962 silicate system wet. *Geology* **41**, 247-250.
963 Molina, J. F., Austrheim, H., Glodny, J. & Rusin, A. (2002). The eclogites of the Marun-Keu complex,
964 Polar Urals (Russia): fluid control on reaction kinetics and metasomatism during high P metamorphism.
965 *Lithos* **61**, 55-78.
966 Mueller, H. J., Schilling, F. R., Lauterjung, J. & Lathe, C. (2003). A standard-free pressure calibration
967 using simultaneous XRD and elastic property measurements in a multi-anvil device. *European Journal of*
968 *Mineralogy* **15**, 865-873.
969 Ricoult, D. L. & Kohlstedt, D. L. (1983). Structural width of low-angle grain-boundaries in olivine.
970 *Physics and Chemistry of Minerals* **9**, 133-138.
971 Rubie, D. C. (1986). The catalysis of mineral reactions by water and restrictions on the presence of
972 aqueous fluid during metamorphism. *Mineralogical Magazine* **50**, 399-415.
973 Sanchidrian, J. A., Ouchterlony, F., Moser, P., Segarra, P. & Lopez, L. M. (2012). Performance of some
974 distributions to describe rock fragmentation data. *International Journal of Rock Mechanics and Mining*
975 *Sciences* **53**, 18-31.
976 Thompson, A. B. (1983). Fluid-absent metamorphism. *Journal of the Geological Society* **140**, 533-547.
977 Wood, B. J. & Walther, J. V. (1983). Rates of hydrothermal reactions. *Science* **222**, 413-415.
978 Yardley, B. W. D. & Valley, J. W. (1997). The petrologic case for a dry lower crust. *Journal of*
979 *Geophysical Research-Solid Earth* **102**, 12173-12185.
980 Zinn, P., Lauterjung, J. & Hinze, E. (1995). Kinetic-studies of the crystallization of coesite using
981 synchrotron-radiation. *Nuclear Instruments & Methods in Physics Research Section B-Beam Interactions*
982 *with Materials and Atoms* **97**, 89-91.

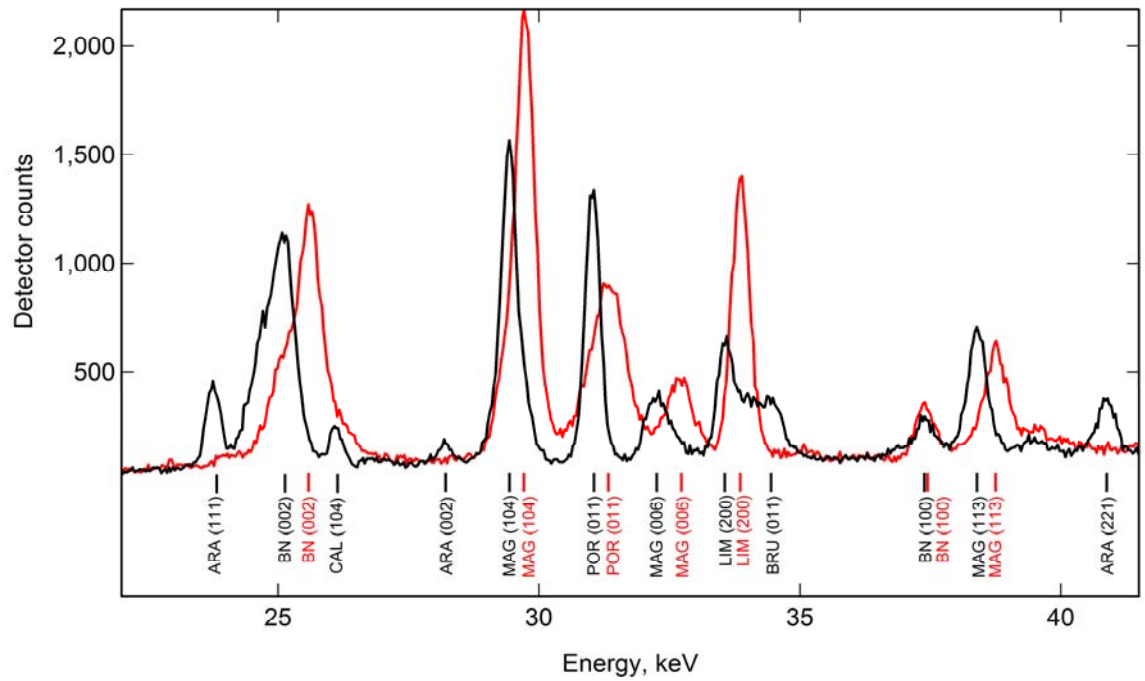

Figure 1

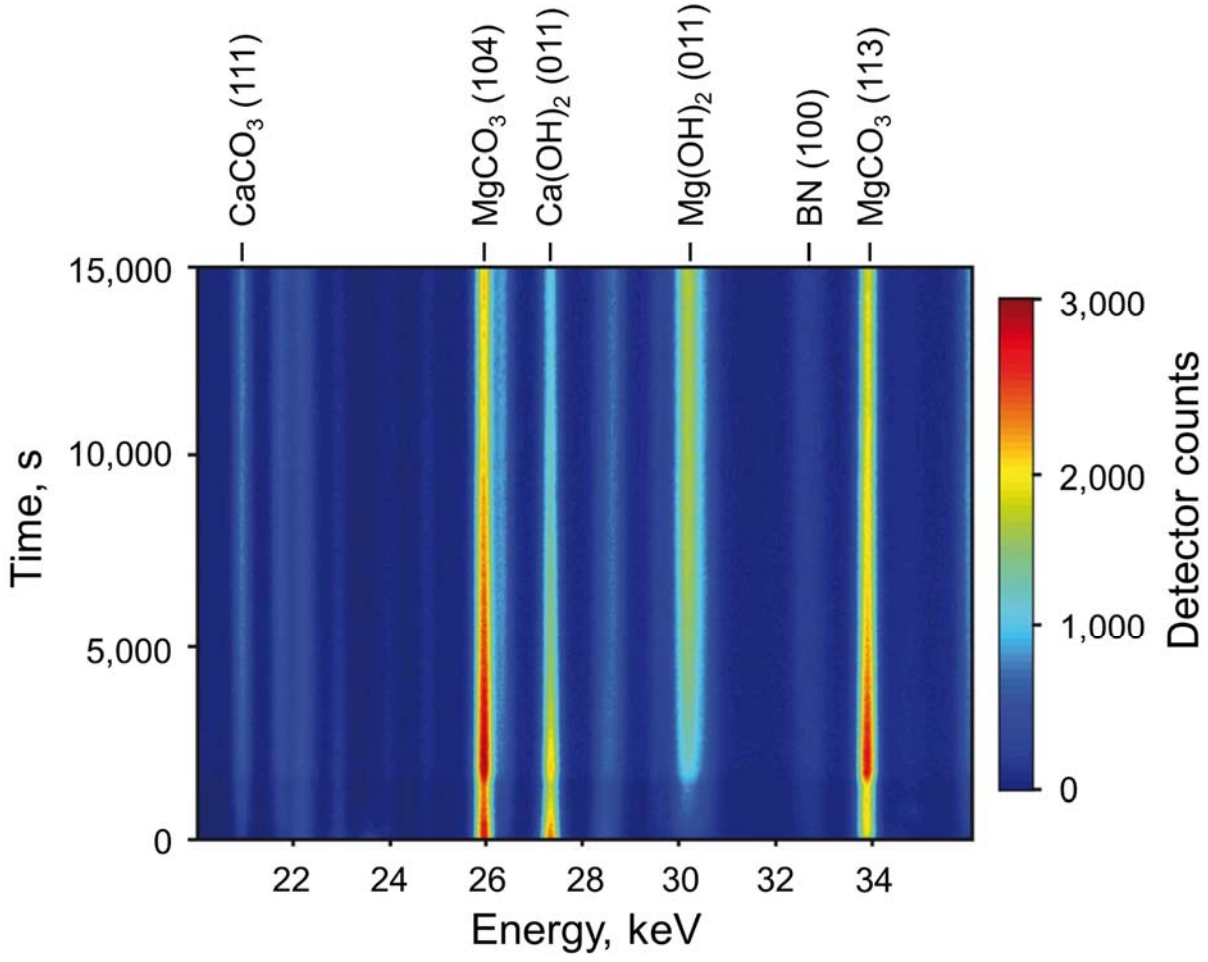

Figure 2

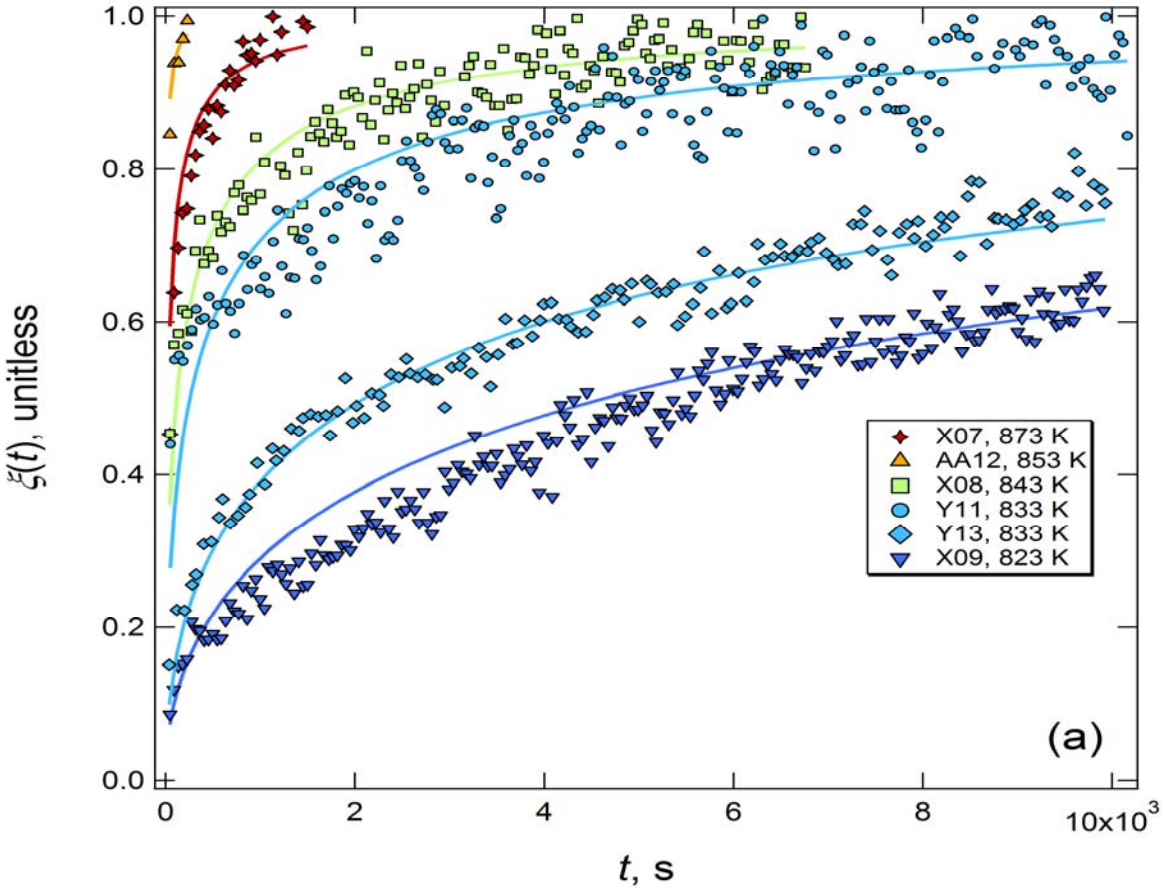

Figure 3a

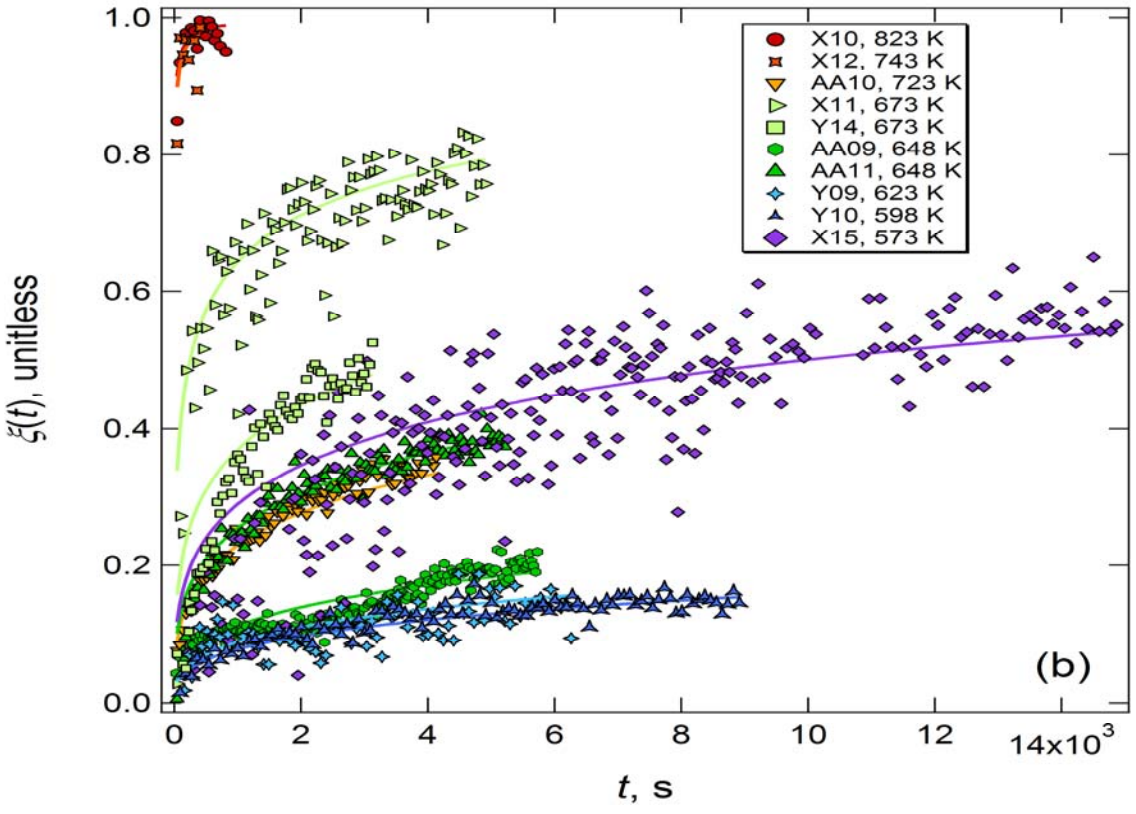

Figure 3b

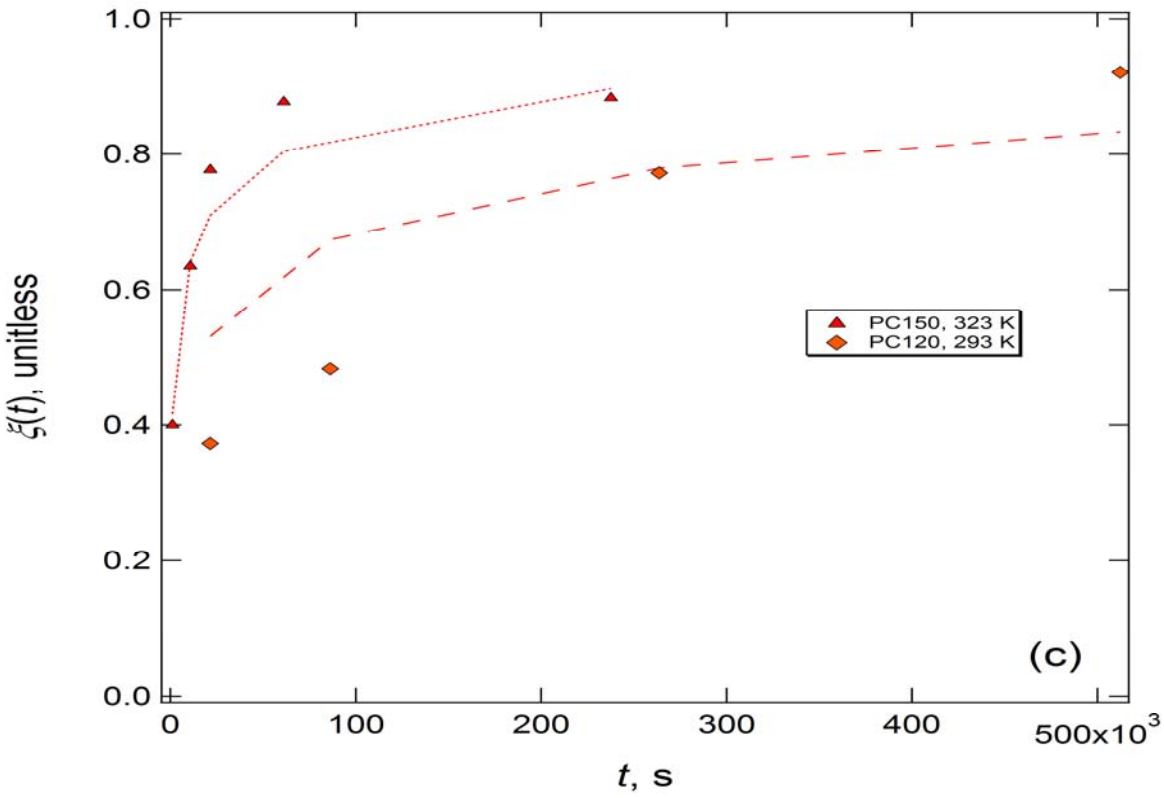

Figure 3c

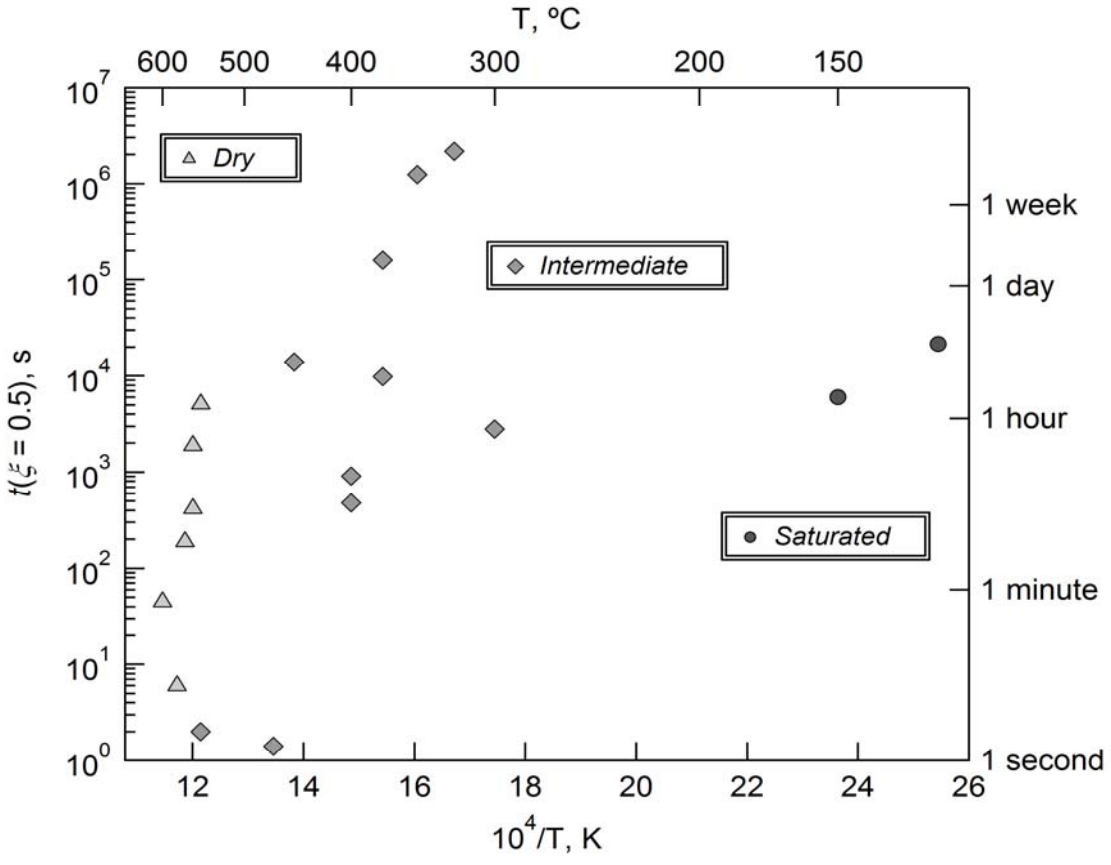

Figure 4

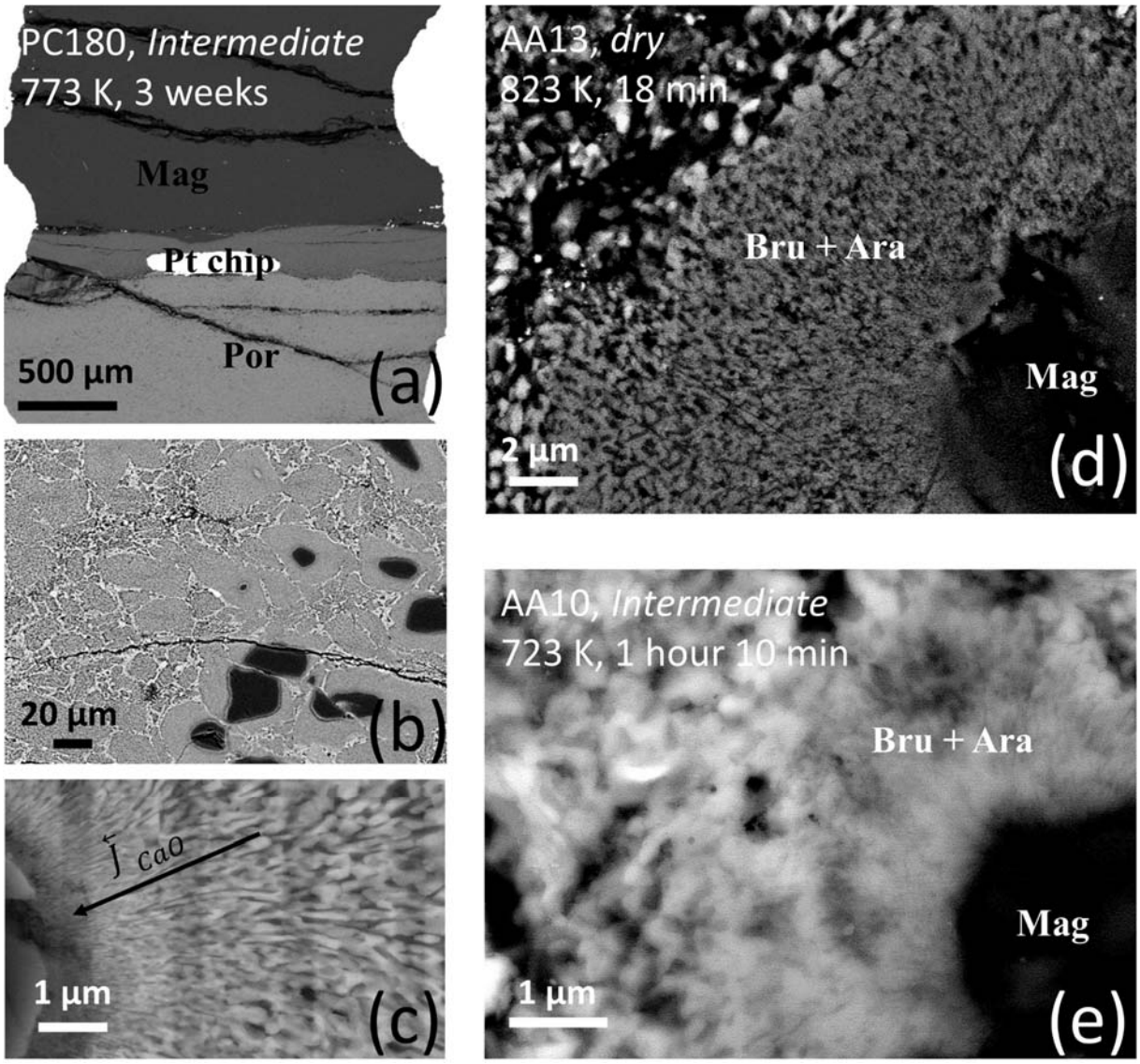
PC180, Intermediate
773 K, 3 weeks
Mag
Pt chip
Por
500 µm
(a)
20 µm
(b)
j_{CaO}
1 µm
(c)
AA13, dry
823 K, 18 min
Bru + Ara
Mag
2 µm
(d)
AA10, Intermediate
723 K, 1 hour 10 min
Bru + Ara
Mag
1 µm
(e)

Figure 5

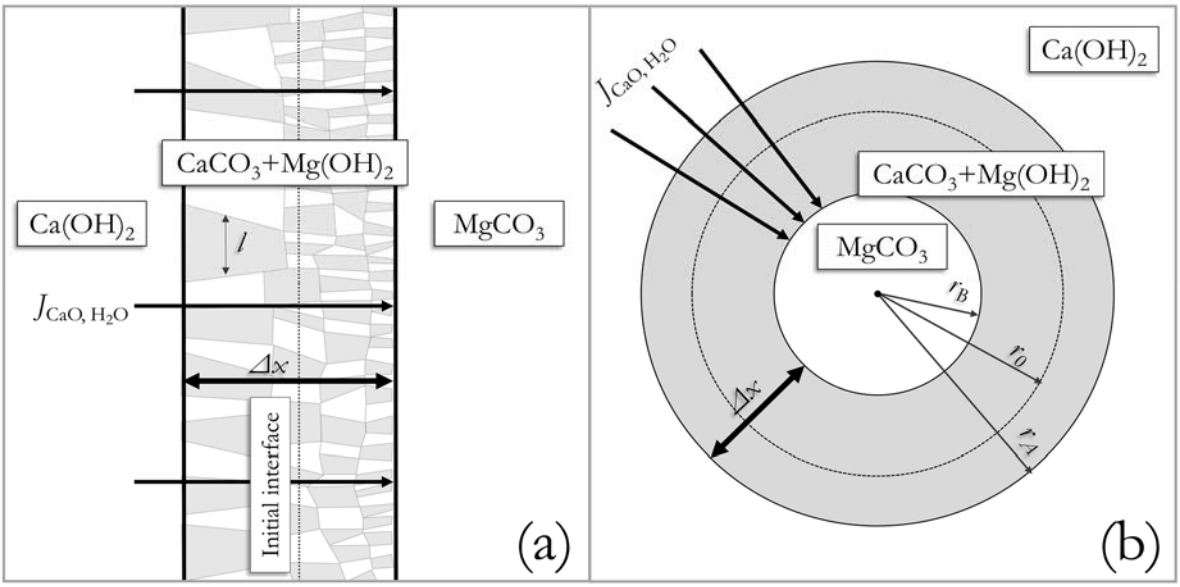

Figure 6

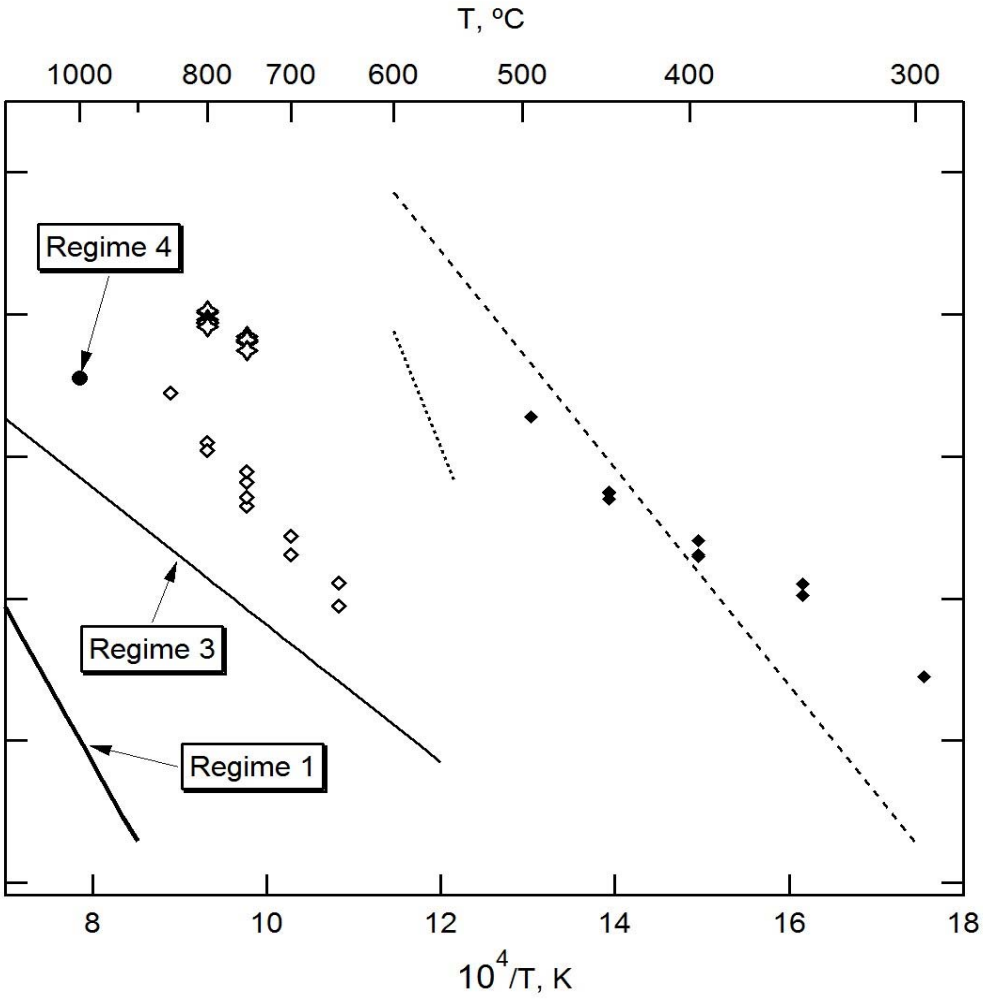

Figure 7a

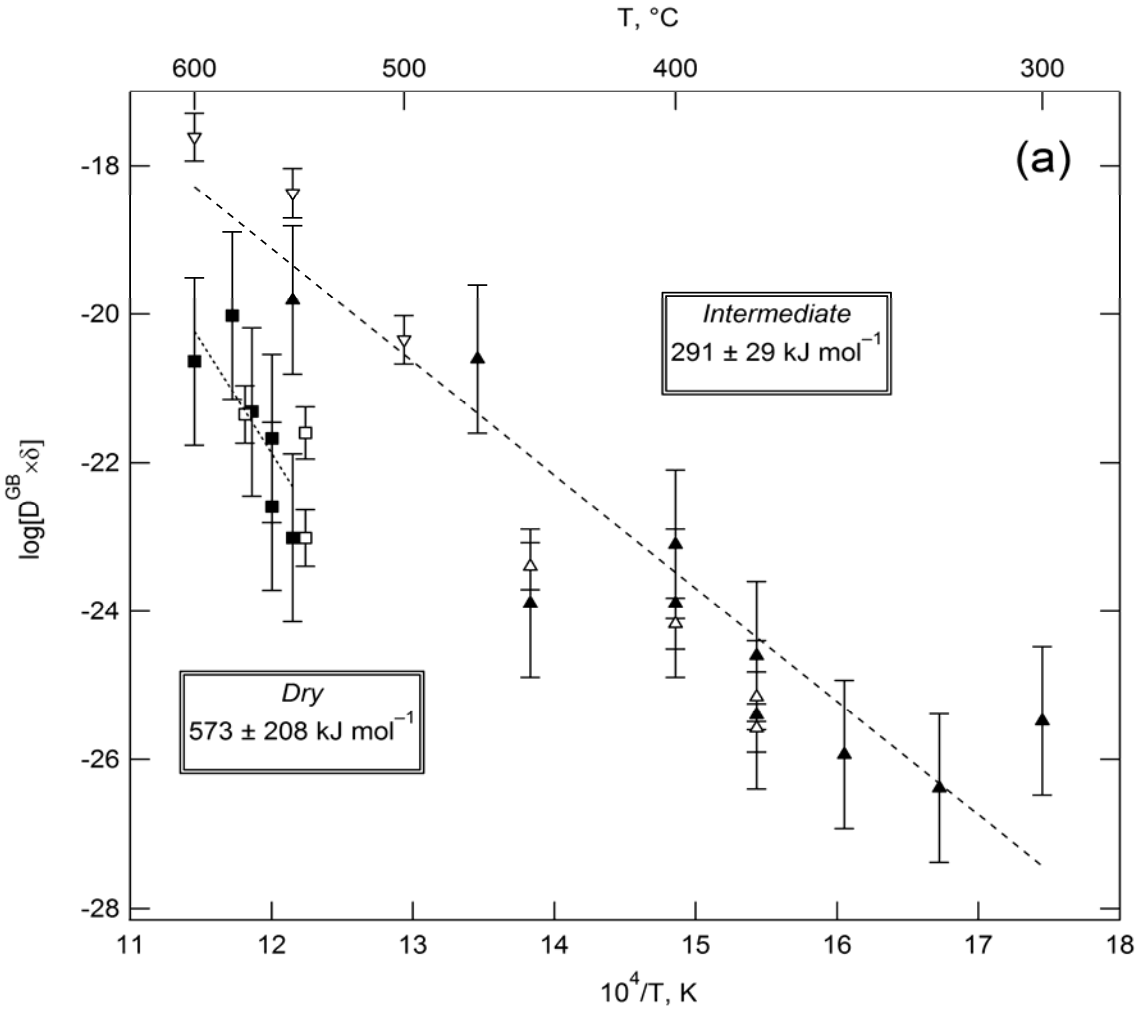
T, °C
600
500
400
300
(a)
-18
-20
-22
-24
-26
-28
log[D^GB×δ]
Intermediate
291 ± 29 kJ mol^-1
Dry
573 ± 208 kJ mol^-1
11
12
13
14
15
16
17
18
10^4/T, K

Figure 7b

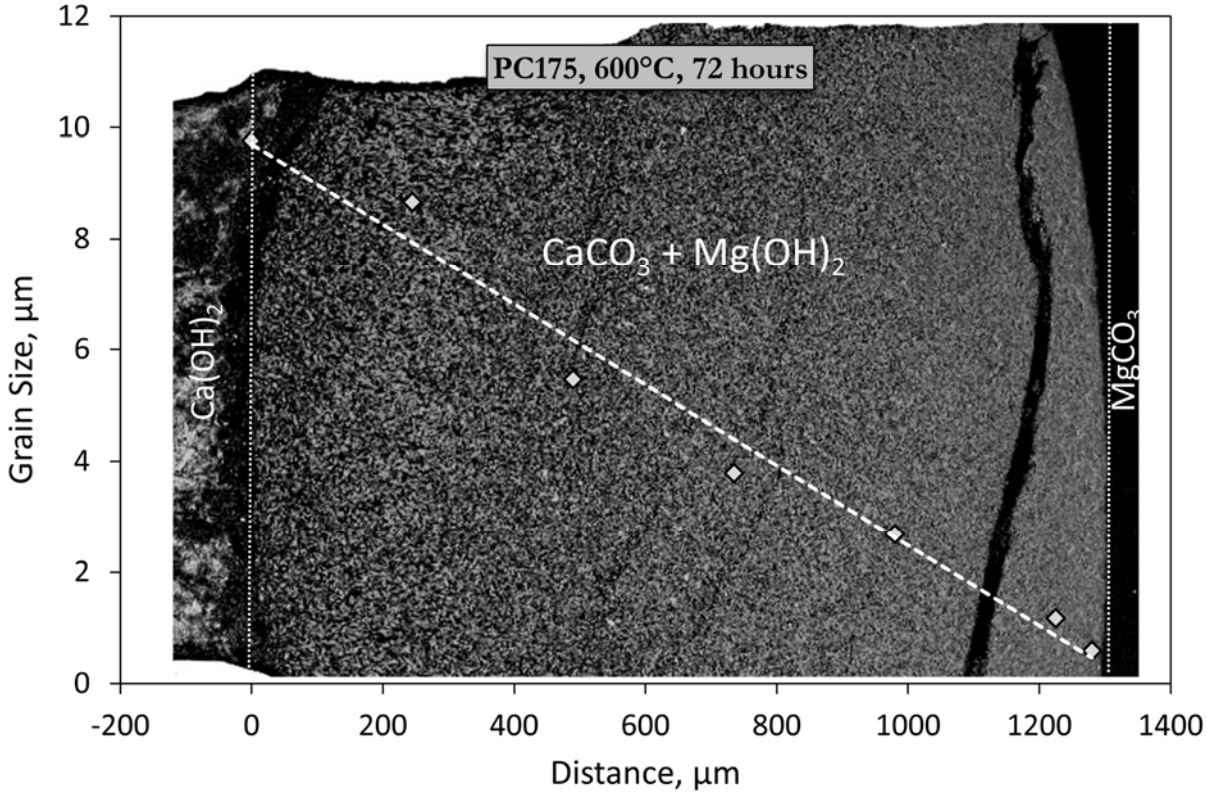
PC175, 600°C, 72 hours
$CaCO_3 + Mg(OH)_2$
$Ca(OH)_2$
$MgCO_3$
Grain Size, µm
Distance, µm
0
2
4
6
8
10
12
-200
0
200
400
600
800
1000
1200
1400

Figure A1

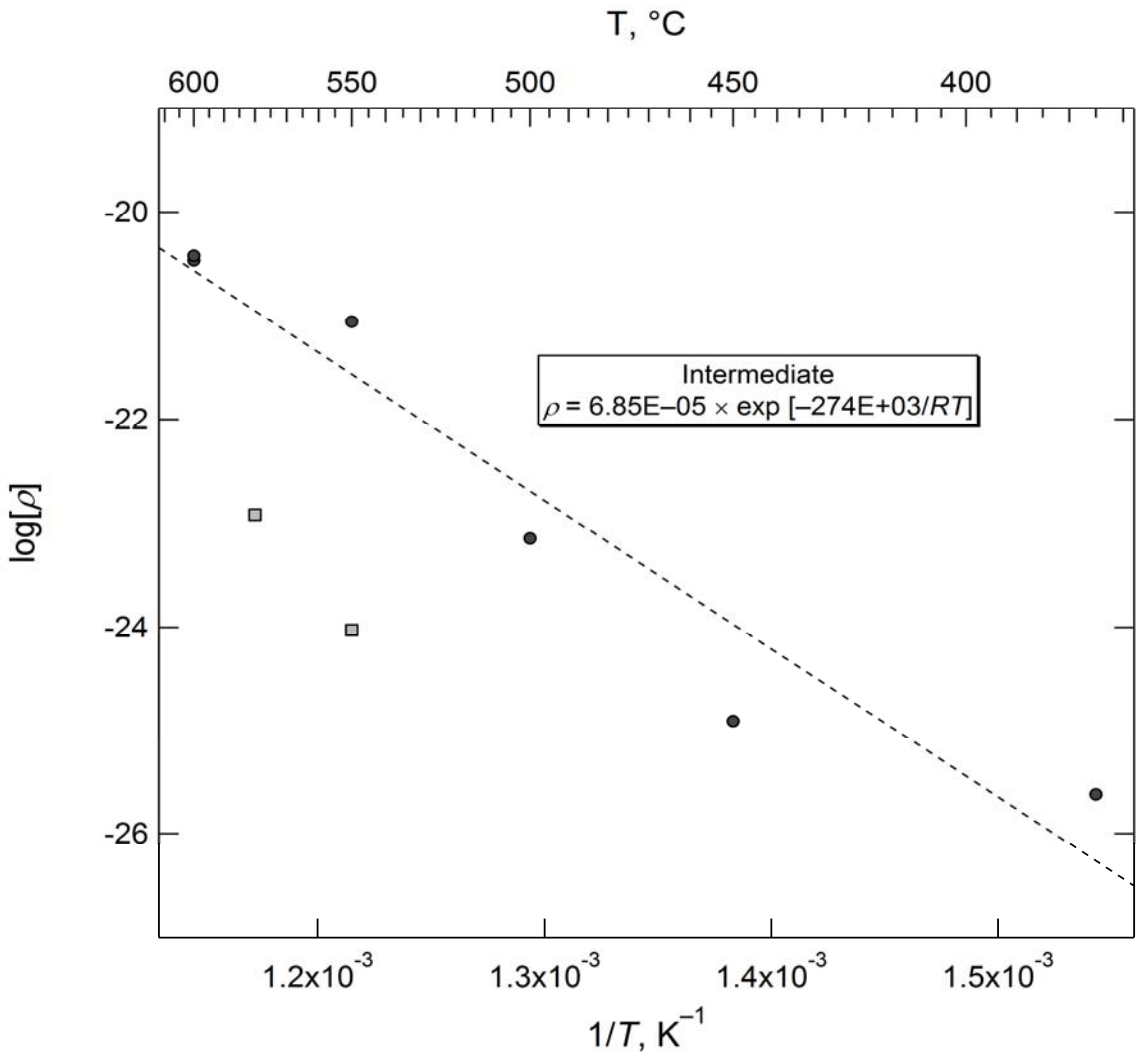
T, °C
600
550
500
450
400
-20
-22
-24
-26
log[ρ]
Intermediate
ρ = 6.85E–05 × exp [–274E+03/RT]
1.2x10-3
1.3x10-3
1.4x10-3
1.5x10-3
1/T, K-1

Figure A2